



Papers Presented at the

28th Annual Summer Intern Conference

August 9, 2012 — Houston, Texas

Papers Presented at the

Twenty-Eighth Annual Summer Intern Conference

**August 9, 2012
Houston, Texas**

2012 Summer Intern Program for Undergraduates
Lunar and Planetary Institute

Sponsored by
Lunar and Planetary Institute
NASA Johnson Space Center



LUNAR AND
PLANETARY
INSTITUTE



Compiled in 2012 by

Meeting and Publication Services
Lunar and Planetary Institute
USRA Houston
3600 Bay Area Boulevard, Houston TX 77058-1113

The Lunar and Planetary Institute is operated by the Universities Space Research Association under a cooperative agreement with the Science Mission Directorate of the National Aeronautics and Space Administration.

Any opinions, findings, and conclusions or recommendations expressed in this volume are those of the author(s) and do not necessarily reflect the views of the National Aeronautics and Space Administration.

Material in this volume may be copied without restraint for library, abstract service, education, or personal research purposes; however, republication of any paper or portion thereof requires the written permission of the authors as well as the appropriate acknowledgment of this publication.

HIGHLIGHTS

Special Activities

June 4, 2012	Tour of the Stardust Lab and Lunar Curatorial Facility	JSC
June 28, 2012	Historical Tour of Mission Control	JSC
July 20, 2012	Tour of the Meteorite Lab	JSC
July 26, 2012	Tour of Robotics and Simulation Lab (Rover, Chariot, Centaur, Spidernaut, and Robonaut)	JSC

Intern Brown Bag Seminars

Date	Speaker	Topic	Location
June 6, 2012	John Shebalin	Planetary Dynamors	Hess Room
June 13, 2012	Allan Treiman	Meteorites: Weirdos from Outer Space	Hess Room
June 20, 2012	Justin Simon	Solar System Chronology	Hess Room
June 27, 2012	Georgiana Kramer	The Link Between Petrology and Remote Sensing	Lecture Hall
July 5, 2012	Interns	Mid-Term Reports	Hess Room
July 9, 2012	Buck Sharpton	Crater Morphology	Hess Room
July 18, 2012	Paul Schenk	Dawn at Vesta	Hess Room
July 25, 2012	Pat McGovern	Geophysics and Volcanology of Mars	Hess Room
July 27, 2012	Don Pettit	Tyranny of the Rocket Equation	Lecture Hall
August 1, 2012	Steve Clifford	Climatic and Hydrologic Evolution of Mars	Hess Room

AGENDA

- 8:00 a.m. BREAKFAST
- 8:25 a.m. Introductory Remarks by Drs. Paul Spudis and Dave Draper
- 8:30 a.m. **JOSHUA BLUMENKOPF, Yeshiva College**
(Advisor: John Shebalin)
Dipole Alignment in a Model Planetary System [#1005]
- 8:50 a.m. **MITALI CHANDNANI, Indian Institute of Technology Roorkee**
(Advisors: David Kring and Georgiana Kramer)
Deep Crustal Lunar Lithologies Exposed in the South-Western Peak Ring of the Schrodinger Basin [#1009]
- 9:10 a.m. **MELISSA JUDSON, State University of New York, Buffalo**
(Advisor: Virgil “Buck” Sharpton)
A Quantitative Approach to Crater Degradation on the Lunar Surface [#1003]
- 9:30 a.m. **JESSICA KALYNN, University of British Columbia**
(Advisors: Patrick McGovern and Georgiana Kramer)
Olivine and Spinel Exposures at Moscoviense and Imbrium Basins [#1006]
- 9:30 a.m. **LISA KORN, University of Massachusetts**
(Advisor: Carlton Allen)
The Gale Crater Mound in a Regional Geologic Setting: Mapping and Probing Surrounding Outcrops for Areas Akin to the Central Mound at Gale [#1001]
- 9:50 a.m. **KATELYN LEHMAN, Texas Christian University**
(Advisors: Walter Kiefer and Georgiana Kramer)
Composition Analysis of the Marius Hills Volcanic Complex Using Diviner Lunar Radiometer Experiment and Moon Mineralogy Mapper [#1007]
- 10:10 a.m. BREAK
- 10:30 a.m. **NICOLE MARIN, Arizona State University**
(Advisors: Kevin Righter and Lisa Danielson)
Metal-Silicate Partitioning of Bi, In, and Cd as a Function of Temperature and Melt Composition [#1012]
- 10:50 a.m. **JAYASHREE SRIDHAR, Hindustan University**
(Advisor: Bonnie Cooper)
Extraction of Meteoritic Metal from Lunar Regolith [#1010]
- 11:10 a.m. **POORNA SRINIVASAN, Rutgers University**
(Advisor: Justin Simon)
Particle Size Distribution of the Allende CV3 Chondrite: A Study that Spans Decimeter to Micrometer Scales [#1008]
- 11:30 p.m. ADJOURN — Lunch provided in the Great Room

(Previously presented during a special session on Wednesday, August 1, 2012)

MOLLY RICHARDSON, Rice University

(Advisor: Julie Moses)

The Effect of Metallicity on the Atmospheric Composition of GJ 436b [#1002]

MATTHEW SMITH, East Tennessee State University

(Advisor: Paul Spudis)

Geological Map of the Nectaris Basin and Its Deposits [#1004]

(Not presenting due to family emergency)

REBECCA JOHNSTON, Brigham Young University

(Advisors: Oliver White and Trudi Hoogenboom)

Crater Chain Classification and Origins on Rhea [#1011]

CONTENTS

Dipole Alignment in a Model Planetary System <i>J. Blumenkopf and J. V. Shebalin</i>	1
Deep Crustal Lunar Lithologies Exposed in the South-Western Peak Ring of the Schrodinger Basin <i>M. Chandnani, G. Y. Kramer, B. Fessler, T. Ohman, and D. A. Kring</i>	4
Crater Chain Classification and Origins on Rhea <i>R. Johnston, O. White, T. Hoogenboom, and P. M. Schenk</i>	7
A Quantitative Approach to Crater Degradation on the Lunar Surface <i>M. M. Judson and V. L. Sharpton</i>	10
Olivine and Spinel Exposures at Moscoviense and Imbrium Basins <i>J. D. Kalynn, G. Y. Kramer, and P. J. McGovern</i>	13
The Gale Crater Mound in a Regional Geologic Setting: Mapping and Probing Surrounding Outcrops for Areas Akin to the Central Mound at Gale <i>L. Korn and C. Allen</i>	16
Composition Analysis of the Marius Hills Volcanic Complex Using Diviner Lunar Radiometer Experiment and Moon Mineralogy Mapper <i>K. M. Lehman, G. Y. Kramer, and W. S. Kiefer</i>	19
Metal-Silicate Partitioning of Bi, In, and Cd as a Function of Temperature and Melt Composition <i>N. Marin, K. Righter, L. Danielson, K. Pando, and C. Lee</i>	22
The Effect of Metallicity on the Atmospheric Composition of GJ 436b <i>M. R. Richardson and J. I. Moses</i>	25
Geological Map of the Nectaris Basin and Its Deposits <i>M. C. Smith and P. D. Spudis</i>	27
Extraction of Meteoritic Metal from Lunar Regolith <i>J. Sridhar and B. Cooper</i>	31
Particle Size Distribution of the Allende CV3 Chondrite: A Study that Spans Decimeter to Micrometer Scales <i>P. Srinivasan and J. I. Simon</i>	34

Dipole Alignment in a Model Planetary System. J. Blumenkopf¹ and J.V. Shebalin², ¹Yeshiva University, Department of Physics, New York, NY 10033 (jblumenkopf@gmail.com), ²NASA Johnson Space Center, Houston, TX 77058 (john.v.shebalin@nasa.gov).

Introduction: The source of the Earth's magnetic field has long been a mystery and although much is now believed to be understood, much remains to be done[1]. The global geomagnetic field cannot be based on permanent magnetization, as the iron in the core is above its Curie temperature, nor is the field due to remnant magnetization imbedded during the Earth's formation, since that field would have died out after ~30,000 years,. Instead, our present view is that the Earth contains a self-exciting dynamo in which electrical currents are driven by turbulent magnetohydrodynamic (MHD) processes in a rapidly rotating liquid iron outer core. Gaining a more complete understanding of the origin and maintenance of the Earth's magnetic field is complicated by the lack of any exact analytic solutions to the highly nonlinear MHD equations (the Navier-Stokes equation with a Lorentz force term, along with Maxwell's equations), and because experimental data is sparse, due to lack of direct access.

Magnetohydrodynamics and Ideal Invariants: The problem of understanding turbulent MHD and its role in the creation of the Earth's mostly dipole magnetic field is approached through numerical simulation as well as statistical mechanics. Numerical simulation is a necessary and useful tool, but it is limited by the inability of computers, now and in the foreseeable future, to fully resolve all the important length scales related to the geodynamo. Nevertheless, computer models provide important data, particularly for validating statistical models of turbulent MHD processes. As a first approximation, the magnetofluid contained in the Earth's core may be assumed to be ideal, that is, non-dissipative, and this allows for a statistical approach based on the invariants of the system. In 3D MHD turbulence, the global invariants include the energy $E = \frac{1}{2} \int (|\mathbf{u}|^2 + |\mathbf{b}|^2) dV$, where \mathbf{u} is the turbulent fluid velocity and \mathbf{b} is the turbulent magnetic field, as well as the magnetic helicity $H_M = \frac{1}{2} \int \mathbf{a} \cdot \mathbf{b} dV$, where \mathbf{a} is the magnetic vector potential ($\nabla \times \mathbf{a} = \mathbf{b}$), and the cross helicity $H_C = \frac{1}{2} \int \mathbf{u} \cdot \mathbf{b} dV$. These invariants allow for canonical ensemble predictions $\langle Q \rangle = \int Q D d\Gamma$, where Q is any modal quantity, Γ is the ensemble phase space and D is an extended Boltzmann probability function (PDF) distribution, $D \sim \exp(-\alpha E - \beta H_C - \gamma H_M)$. This statistical formulation can then be tested and, if necessary, amended through numerical simulation.

Numerical simulations, in turn, proceed by discretizing the problem into modes, using the Fourier Trans-

form in the periodic box case and spherical harmonics in the spherically bounded case. Although the initial statistical theory [2] predicted that all spatial modes would be zero-mean random variables, numerical studies clearly showed that the largest-scale modes, which contain most of the energy, were not zero-mean but instead demonstrated 'broken ergodicity' [3,4].

Hybrid Statistics: Coherent energy in the low modes is associated with this lack of ergodicity, so that the quasistationary dipole moment in a turbulent magnetofluid is due to this lack of ergodicity, but no explanation has been put forward for its approximate alignment with the rotation axis until recently[5]. While the magnetic helicity is only exactly conserved in a case without rotation, in a rotating, turbulent magnetofluid $\dot{H}_C = H_C/E$ appears to fluctuate about a stationary value. Using \dot{H}_C as a quasi-invariant in the PDF $D = \prod_m D_m$, where the D_m are modal PDF factors, leads to a 'hybrid statistics'[5] where modes $m = 0$ (axisymmetric with the rotation axis) have $\dot{H}_C \neq 0$, while non-axisymmetric modes $m \neq 0$ have $\dot{H}_C = 0$. The expected dipole angle θ_D can then be obtained from the ratio between the predicted energies of the $m = 0$ and $m \neq 0$ modes. (A similar hybrid statistical mechanics has been used to explain anisotropy in MHD turbulence in the presence of an externally applied mean magnetic field[6].)

Hybrid statistical mechanics involves the entropy functional[3,4], given by $\sigma(\varphi) = -\langle \ln D \rangle$ or:

$$\sigma(\varphi) = -\sum_m \langle \ln \{ D_m[\alpha_m(\varphi), \beta_m(\varphi), \gamma_m(\varphi)] \} \rangle. \quad (1)$$

The entropy functional $\sigma(\varphi)$ has only one minimum, which can be found numerically. Finding the minimum precisely is, in fact, a challenge needing special methods, and the development of such methods was the specific goal of this project. The entropy functional $\sigma(\varphi)$ depends on the 'inverse temperatures' α_m , β_m , and γ_m , which are themselves functions of just one variable φ , the magnetic energy[5]. A numerical search algorithm starts by moving up an amount $\Delta\varphi$ from the lowest value in its range ($\varphi = E/2$) and then stops when $\sigma(\varphi)$ begins increasing or ceases to have real values; the algorithm then sets $\varphi - 2\Delta\varphi$ and $\Delta\varphi \rightarrow \Delta\varphi/10$, and moves forward again, repeating the process until $\Delta\varphi = 0$ to machine accuracy, at which point $\varphi = \varphi_0$ and the $\sigma(\varphi)$ has a minimum $s = \sigma(\varphi_0)$, which is the entropy of the model system. This algorithm was implemented in a Fortran code and used to find φ_0 for given values of \dot{H}_C and \dot{H}_M . For a constant value of

\hat{H}_M , our results show a lack of dipole alignment for low \hat{H}_C , but then as \hat{H}_C increases, the expected dipole angle θ_D decreases, until a smallest value of θ_D appears at the end of the range of \hat{H}_C . As Figure 1 shows, increasing \hat{H}_M shifts the minimum value of θ_D to lower values of \hat{H}_C . Using data from numerical simulations of periodic-box MHD turbulence (which allows for fast-Fourier transforms and high computational speed) in a dissipative case with nonequilibrium initial conditions and no forcing, values for \hat{H}_M and \hat{H}_C are obtained with respect to a characteristic time, as seen in Figure 2. The Ohmic decay time for a real Earth (as opposed to a low-resolution numerical simulation) is $\sim 30,000$ years; this is much shorter than the realistic viscous decay time by a factor of a million, but in the simulation, viscous and Ohmic decay times are about the same in terms of dimensionless simulation time. However, there is no direct connection between simulation time and characteristic time, because simulation time is faster than real time since simulation viscosity and magnetic diffusivity are much larger than the real Earth values. Nevertheless, the figures show what we believe to be the qualitative behavior we expect in the geodynamo.

Conclusion: Here, we focused our research on a statistical theory of planetary dynamos based on ideal MHD turbulence theory and, in particular, implemented an essential algorithm for finding the expectation value of magnetic energy and hence the entropy of the model system. The statistical model based on the ideal invariants of MHD turbulence gives us important, qualitative insight into dipole alignment in planetary dynamos, especially when used in conjunction with numerical simulations. The ideal theory can be applied to slowly decaying MHD turbulence, but needs to be further extended to account for possible variations due the specific rotation rates of the various planets of our solar system. Numerical simulations, in turn, will benefit from future increases in computational power and this will also help us better understand the fundamental nature of planetary dynamos.

References:

- [1] Olson, P. (2009), *Core Dynamics*, Elsevier, NY.
- [2] Frisch, et al., (1975), *J. Fluid Mech.*, 68, 769–778.
- [3] Shebalin, J.V. (1989), *Physica D*, 37, 173–191.
- [4] Shebalin, J.V. (2009), *Phys. Plasmas*, 16, 072301.
- [5] Shebalin, J.V., (2012) *EPS-ICPP Plasma Conf.*, P1.161, Stockholm, July 2-6.
- [6] Shebalin, J.V., *Rad. Effects Defects Sol.* 166, 774–788, 2011.

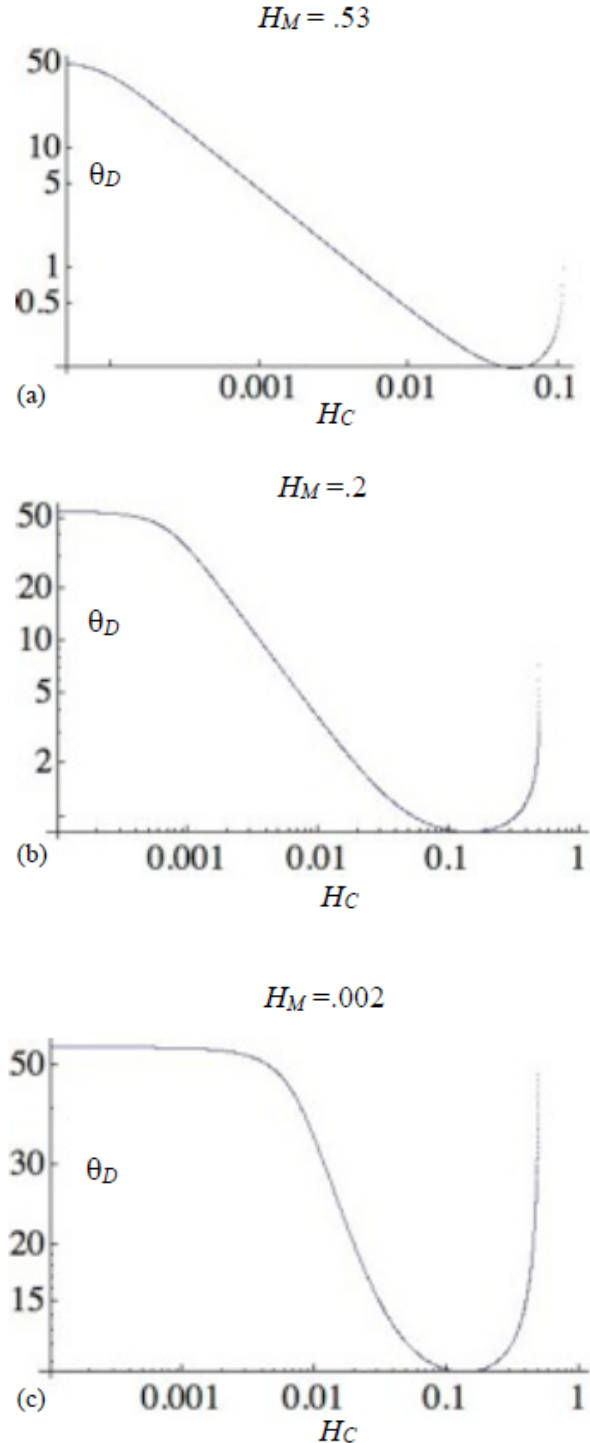


Fig. 1. Plots of dipole angle versus H_C for various values of H_M .

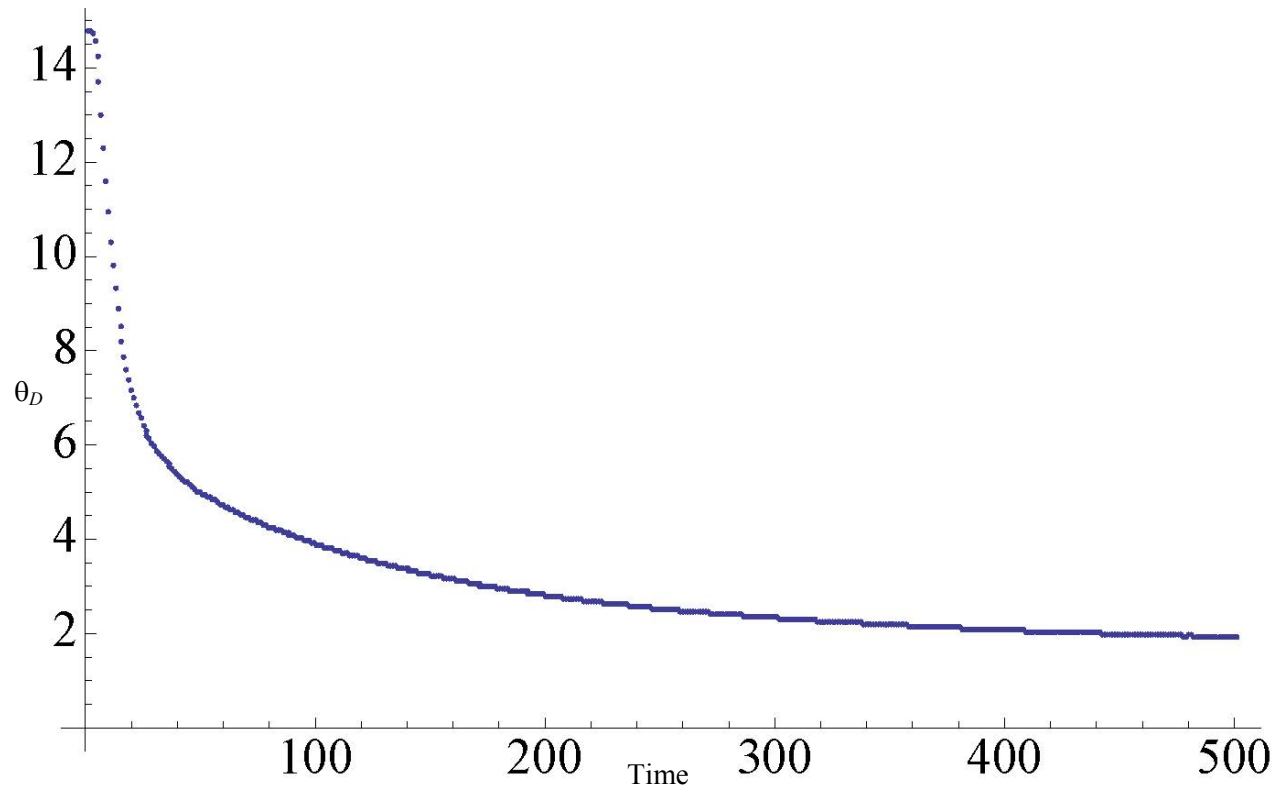


Figure 2. Plot of dipole angle versus time for a numerical simulation of rotating, dissipative, homogeneous MHD turbulence, starting with nonequilibrium initial conditions. The effective normalized cross helicity is $\hat{H}_C = 0.02655$. Since $d\hat{H}_M/dt > 0$ for rotating, dissipative MHD turbulence, \hat{H}_M increase with time and this leads to increased alignment with time. The qualitative meaning of this is that the geodynamo (or, in general, any planetary dynamo), is suddenly stirred up by episodic inner core condensation, for example, which corresponds to the initial conditions of a simulation; then, the turbulent magnetofluid relaxes to a quasi-equilibrium in which energy slowly decays with time, with the normalized magnetic helicity \hat{H}_M steadily increasing. The process repeats itself either periodically or sporadically, and if the initial disturbance is large enough, the direction of the dipole part of the magnetic field may reverse itself. Smaller disturbances, in turn, may be associated with so-called magnetic excursions in which the dipole field has a relatively large fluctuation, but does not reverse itself.

DEEP CRUSTAL LUNAR LITHOLOGIES EXPOSED IN THE SOUTH-WESTERN PEAK RING OF THE SCHRÖDINGER BASIN. M. Chandnani^{1,2}, G.Y. Kramer², B. Fessler², T. Öhman² and D.A. Kring²,
¹Department of Earth Sciences, Indian Institute of Technology, Roorkee 247667, India (mitali.iitroorkee@gmail.com), ²Lunar and Planetary Institute, 3600 Bay Area Boulevard, Houston, TX 77058

Introduction: The Schrödinger basin (Fig. 1), centered at 75°S, 132.4°E, is a complex impact structure with a 320 km diameter rim and a 150 km diameter inner peak ring [1]. It is believed to be an early Imbrian-aged impact feature [2, 3] that is the second youngest multi-ring impact basin-forming event on the Moon. Thus, it is one of the best preserved features of its size and age.

Schrödinger basin lies within the main topographic ring of the South Pole-Aitken (SPA) basin, which is the largest and oldest impact basin on the Moon. Schrödinger, superposed at or near the rim of SPA, is thought to excavate material from depths of ~10-30 km [4, 5] in the modification zone of SPA. Therefore Schrödinger's rim, peak ring and floor materials can be used to determine the composition [6] and a substantial cross-section of the south polar crust. Schrödinger's peak ring is observed to be mineralogically diverse and calculated to have uplifted material from the crust-mantle interface, i.e., 50 km depth [7]. This makes it a compelling candidate for lunar surface operations. It is being targeted as a potential landing site for future human explorations on the Moon [8].

The purpose of this paper is to create a geological map of the south-western peak ring of the Schrödinger basin and interpret the exposed south polar crustal lithologies and structural features in this area. Generation of a geologic map and characterization of the peak ring's geology can be used by studies as a resource for future mission planning.

Methods: To obtain a high resolution image mosaic of the target area (the south-western peak ring), the ACT-REACT Quick Map tool [9] was used to locate high resolution Lunar Reconnaissance Orbiter Camera Narrow Angle Camera (LROC NAC) imagery centered at 75.34°S, 124.87°E.

Generating a mosaic with resolution of 0.72 metres from individual NAC strips was done using ISIS software [10]. This involved their conversion to .cub files, computation of ground distances and photometry, radiometric corrections, conversion of the strips to map projected files and generation of a seamless mosaic (Fig. 2) from the .cub files.

The mosaic was used as a basemap layer in ArcGIS 10 software. The mineral map (Fig. 3) derived from the M³ satellite data [7] for the area was co-registered with the mosaic. These two layers were

used as references to identify and map all the lithological contacts and structural features in the south-western peak ring.

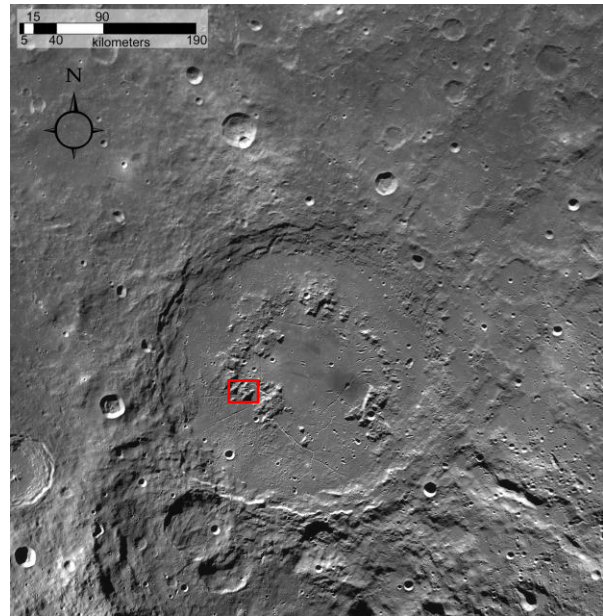


Figure 1. An LROC Wide Angle Camera (WAC) mosaic of the Schrödinger Basin with the region of interest (ROI) shown by the red box.

Results and Discussion: The geological map (Figure 4) shows the lithologic diversity of the peak ring and its division into three parts separated by two normal faults. A graben internally splits the middle portion from the east.

a) Structural features: A striking pattern of faults cut across the peak ring and offset the sequence of lithologies. The two faults (1 and 2, fig. 4) divide the peak ring into three parts, which is evidenced by topography and the occurrence of adjacent norite blocks in the two upper divisions and troctolite hills in the middle and lower divisions. It could have been produced by uplift of the center of the basin. These faults tend to be radially aligned with the center of the basin in this case. A graben (H in fig. 4) passes through the middle division of the peak ring so that it separates the respective troctolite and norite boulders. These faults can provide a clue to the ancient stress field and the origin of deformation [3]. The faulting may be the result of slight isostatic rebound of the center of the

basin that perhaps occurred shortly after emplacement of the melt sheet [3].

b) Petrology: The LROC NAC mosaic and M^3 mineralogy map show that the south-western peak ring is mineralogically diverse with three dominant rock types: norite, troctolite, and anorthosite. All three lithologies are comparable in abundance and visible as boulders on the NAC mosaic. Norite is dominant in the northernmost division, troctolite in the southernmost part, and anorthosite is scattered throughout the peak ring in the form of either pure anorthosite or pyroxene-bearing anorthosite. A cluster of hummocks having pyroxene-bearing anorthosite was also observed in the southernmost division.

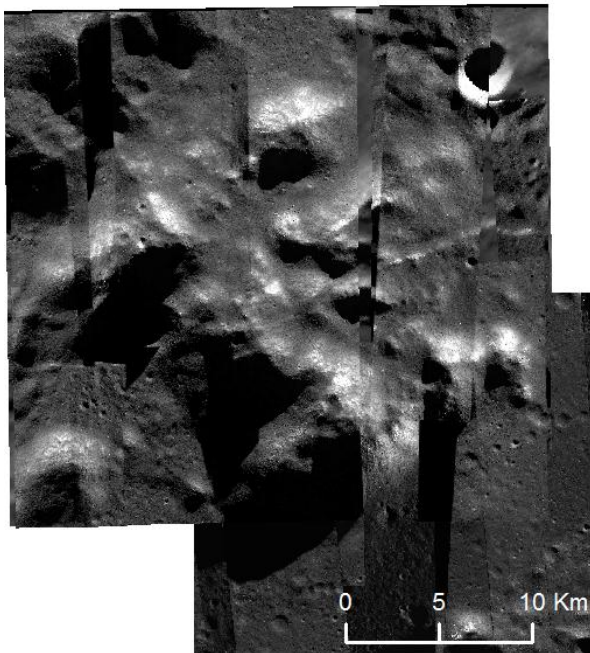


Figure 2. An LROC NAC mosaic of the south-western peak ring of the Schrödinger basin created in ISIS.

With respect to albedo, norite was observed to be the darkest rock. Anorthosite is expected to be brighter than troctolite, because it contains the lower-albedo mineral olivine. However, it was very difficult to distinguish between adjacent anorthosite and troctolite in the NAC mosaic. Their comparably high albedos are probably due to direct sunlight from the north-east direction. Only M^3 spectra could make the distinction between the two lithologies.

In the case of norite, comparing figures 2 and 3 shows that norite has a unique albedo and is clearly distinguishable from the surrounding lithologies, except for the eastern side of the huge mound in the

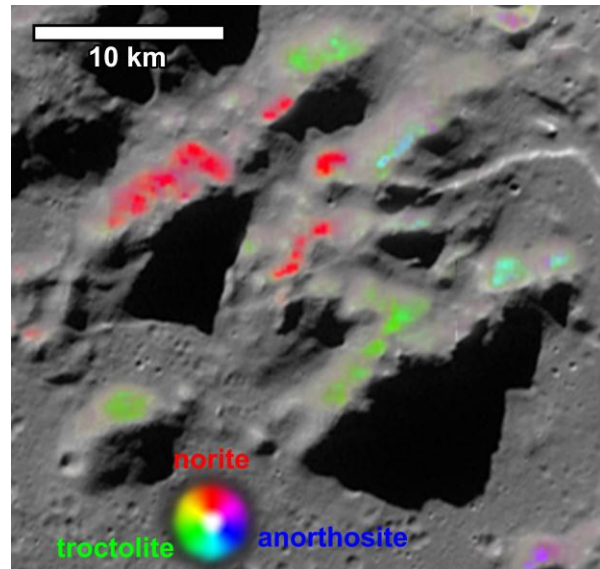


Figure 3. M^3 mineralogy map of the ROI from [7].

northernmost division where low-albedo norite (from M^3 spectra) dominates the composition of the regolith covering making it look darker.

Also, in the northern part of the northernmost division, norite was observed to be on the edge of the troctolite hill A (Fig. 4). This is because the downslope weathering of norite from block B (Fig. 4) caused the boulders to get scattered to a long distance (evidenced by a trail at location C from figure 4). But the boulders are not visible because of the shaded slope and the weathering of troctolite boulders onto it. The norite mounds I and J (fig. 4) appear to have been separated by the graben and so may have been once a part of a large norite block.

As far as troctolite is concerned, spectra from the northern division exhibits spectral features of olivine and plagioclase. On heading south, it was observed that the rock becomes olivine rich (block D in figure 4), based on the lack of an observable plagioclase feature. However, the rock is still inferred to contain plagioclase, although its spectral signature cannot be observed due to the spectral dominance of olivine over plagioclase [7]. An increasing amount of plagioclase can be seen in the spectra of the troctolite hills E and F (fig. 4). Hills E, F and G exhibit similar spectral features. But hills F and G are disconnected from block E due to the presence of the graben H. All these mounds (E, F and G) are continuous with patches of dark regolith in between. Despite the greater number of shadows in the southernmost part, troctolite was found to be observable in some locations, because of its high albedo even in dark areas and from M^3 spectra.

Anorthosite occurs as pure anorthosite traces in the middle and southernmost divisions and as massive cumulates of pyroxene-bearing anorthosite in all three divisions. However, three different transitions of lithologies were observed on the map (Fig. 4): pyroxene bearing anorthosite to norite (location K) in the northernmost division, gradation from 2 to 5% pyroxene bearing anorthosite to pure anorthosite to olivine-rich troctolite (location L) in the middle division, and troctolite to pure anorthosite to troctolite again (location M) in the east of southernmost division. Some pyroxene-bearing anorthosite also occurs in a crater east of the peak ring (upper right of figure 4).

All mounds containing the three rock types have rough surfaces at places where the slope grade decreases due to an increased accumulation of regolith. Most of the craters on this surface are worn away by slumping of material. However, some smooth patches can be seen in flat areas that preserve a cluster of fresh craters due to the absence of slumping.

Some locations indicated as “unknown” in figure 4 have been delineated where outcrops could be seen in the NAC mosaic, but the mineralogy could not be identified because they are in shadow in the M³ data.

The light grey area delineated in the map is the peak ring regolith. It is distinguishable from the surrounding regolith on the basis of change in slope and a rougher texture.

Conclusion: The south-western peak ring of Schrödinger basin is composed of 3 major lithologies: norite, troctolite, and anorthosite, which occur as isolated massive cumulates. The occurrence of large amounts of troctolite formations observed at various places in the peak ring either represent a primary igneous lithology or a comingling of cumulate olivine and plagioclase during peak ring formation. The lithologies can be used as proxies in providing information about the lunar interior, i.e., the crust-mantle interface, as it has been found to contain uplifted material from that depth (50 km). This observation, alongwith that of the large size of the boulders, supports the lunar magma ocean theory [11, 12].

The map shows that some structural boundaries, like faults and graben, can be seen cutting through the peak ring. The faults divide the peak ring into three divisions demonstrated by the blocks of the same lithology that are offset from each other in adjacent divisions. Likewise, the graben (H in fig. 4) cuts through the respective troctolite and norite boulders in the middle division. The latter faults may have been formed during the isostatic uplift of the center of the basin.

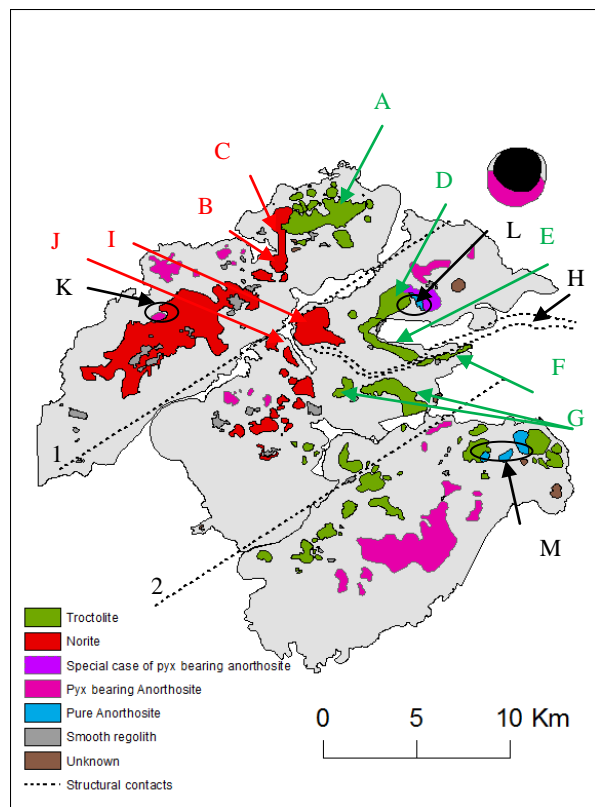


Figure 4. Generated map of the south-western peak ring of the Schrödinger basin in ArcGIS 10.

References: [1] Pike R.J. and Spudis P.D. (1987) *Earth, Moon and Planets*, 39, 129-194. [2] Wilhelms D.E. et al. (1979) *Geol. Surv. Map I-1162*. [3] Shoemaker E.M. et al (1994) *Science*, 266, 1851-1854. [4] Cintala M.J. and Grieve R.A.F. (1998), *Meteoritics and Planetary Sci.*, 33, 889-912. [5] Ivanov B.A. (2005), *Solar System Research*, 39, 381-409. [6] Mest S.C. (2011), *The Geological Society of America Special Paper 477*, 95-115. [7] Kramer G.Y. et al (2012), *2nd Lunar Highlands Crust Conf.*, Abstract #9013. [8] O’Sullivan K.M. et al (2011), *GSA Special Pub. 477*, 117-127. [9] LROC :: ACT-REACT QuickMap. (n.d.). Retrieved from <http://target.lroc.asu.edu/da/qmap.html> [10] USGS Isis: Planetary Image Processing Software (05/19/2012). Retrieved from <http://isis.astrogeology.usgs.gov> [11] Smith J.V. et al (1970), *Proc. Apollo 11 Lunar Sci. Conf.*, 1, 897-925. [12] Wood J.A. et al (1970), *Proc. Apollo 11 Lunar Planet. Sci. Conf.*, 965-988.

CRATER CHAIN CLASSIFICATION AND ORIGINS ON RHEA. R. Johnston¹, O. White², T. Hoogenboom², and P. M. Schenk². ¹Brigham Young University, Provo, Utah 84602 (becky.johnston@byu.edu), ²Lunar and Planetary Institute, Houston, Texas, 77058 (white@lpi.usra.edu, hoogenboom@lpi.usra.edu, schenk@lpi.usra.edu)

Introduction: Crater chains are defined as linear strings of closely spaced, roughly similar-sized, aligned circular depressions, and were first identified on the Moon from Lunar Orbiter and Apollo imagery [e.g. 1, 2], and later on the Galilean moons Ganymede and Callisto from Voyager and Galileo imagery [3, 4]. Lunar chains are interpreted to be formed of secondary impact craters ejected from a primary source crater [5], yet after the impact of the tidally disrupted comet Shoemaker-Levy 9 into Jupiter in 1994, it was postulated that impact of such disrupted cometary fragments into planetary surfaces was another viable mode of formation of crater chains [4]. A survey of crater chains on Ganymede and Callisto yielded 11 chains (or catenae) that could not be linked to any potential source basin, and which were labeled ‘anomalous’ and considered to be of possible cometary origin [4]. A possible third, endogenic mode of origin is formation through subsidence caused by tectonic activity on the parent body [4]. Identifying crater chains formed by secondary impacts is important for dating planetary surfaces, as distinguishing primary and secondary impacts allows more reliable crater counts to be obtained; determining a cometary origin for a chain allows the properties of the original comet to be deduced [3].

The observations in the Jovian system prompted speculation of the existence of crater chains in the Saturnian system and their mode of origin; only a few, putative crater chains have been observed on Saturn’s satellites in Voyager imagery [4]. Theoretically, the existence of cometary chains formed by a Shoemaker-Levy 9-sized event is unlikely because the periastron of the orbit that is necessary to achieve tidal disruption of such a comet is actually inside Saturn due to the planet’s lower density [4, 6].

The Cassini orbiter, which arrived at the Saturnian system in 2004, has provided much more extensive coverage of its satellites, and at greater resolution, than Voyager, making possible a focused study of crater chains in this system. This study focuses on Rhea, one of the most heavily cratered of the satellites. Cassini has obtained nearly global coverage of Rhea, with 75% coverage at better than 400 m/px. The aim of the study is to identify crater chains on Rhea and subdivide them into those that can confidently be linked to source basins, and those interpreted to be of a cometary or tectonic origin. The results will be used to test the assertion that cometary impacts should be rare in the Saturnian system.

Methods: The initial step involved identifying as many crater chains as possible within the Voyager and Cassini image data sets which include 1032 images, 31 of which are from Voyager. In order for a group of craters to be classified as a chain, four or more craters aligned roughly linearly had to be observed. 66 such chains were identified with a high degree of confidence, and each was catalogued into one of three morphological classes: pearls, grooves, and needles (see Fig. 1). Pearls comprise a chain of discrete, mostly circular impact craters that do not overlap. Grooves are essentially linear troughs, but in which ‘bulges’ representing individual impacts can still be discerned; Any discrete impact craters in the chain are elongate. Needles are linear troughs with no identifiable individual impacts.

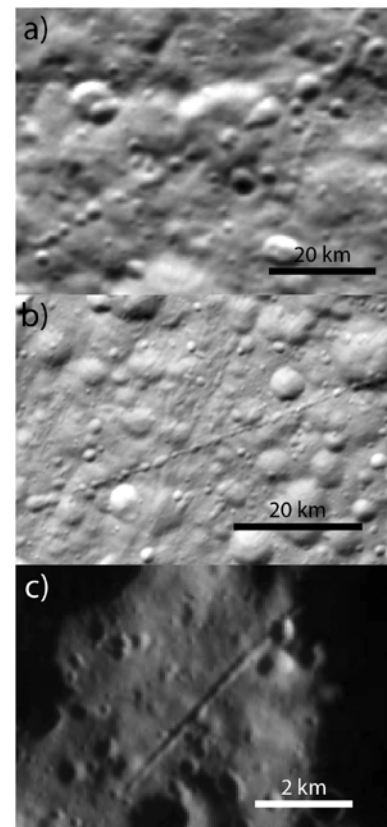


Figure 1. Crater chain morphologies (a) Pearl chain located at 5.5°S, 63.1°W. (b) Groove chain located at 33.5°N, 167.8°W. (c) Needle chain located at 4°N, 45.7°W.

The classification system is subject to image resolution and solar incidence angle. The same chain may appear to have a different morphology in two different

images. In such cases, the morphology as it appears in the highest resolution image is recorded.

The catalogue records the center coordinates, azimuth, length, maximum width, and morphology type of each chain. For each chain, the coordinates of several points along the chain are used to define a small circle that would represent the groundtrack of the path taken by the ejecta, assuming the chain is comprised of secondary impact craters. This path is then scrutinized for potential source craters that overlap with it. Secondary impactors typically occur radially from the original impact, yet in some cases may even occur tangentially to the primary. To account for this, craters are sought that the small circle not only passes through but are near enough, given the standard deviation, to be tangential candidates.

The likelihood of a primary crater being the source of a chain also depends on the relative sizes of the source crater and the chain. A scaling law previously applied to lunar secondaries [7] was used to determine the smallest possible size of the primary impactor from the largest crater diameter in the chain: $D_2 \approx 0.14D_p^{0.77}$, where D_2 is the diameter of the largest crater in the chain and D_p is the smallest diameter of the primary basin. In addition, the calculated value of D_p was relaxed by 80% in order to account for variance in impact crater behavior. The chain should also be sufficiently proximal (taken to be within 90°) of the source basin.

In order for a source crater to be confidently identified, both the small circle fit, scaling law fit and proximity should be satisfied. While a more subjective criterion, the preservation state of the chain and source crater should also be similar. If no qualified candidates exist, the chain is termed anomalous.

Results: The locations of all 66 catalogued chains are shown in Fig. 2. Fig. 3 and Table 1 collate statistics for various properties of each chain class.

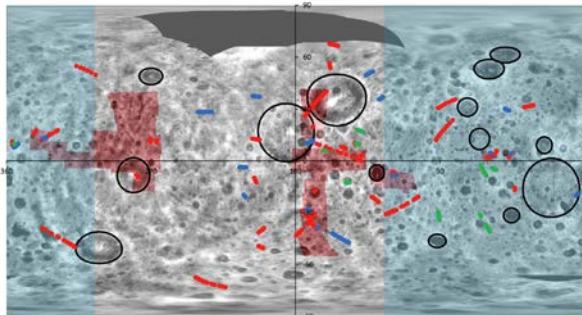


Figure 2. Global distribution of crater chain morphologies on Rhea, superimposed on a digital elevation model. Pearls are green, grooves are red, and needles are blue. The rims of craters >100 km in diameter are highlighted in black. The sub-Saturnian point is located at 0°N , 0°E . The blue area highlights the hemisphere where cometary impacts are

expected based on observations at the Galilean moons [4]. The red areas highlight Cassini coverage obtained at better than 0.2 km/px.

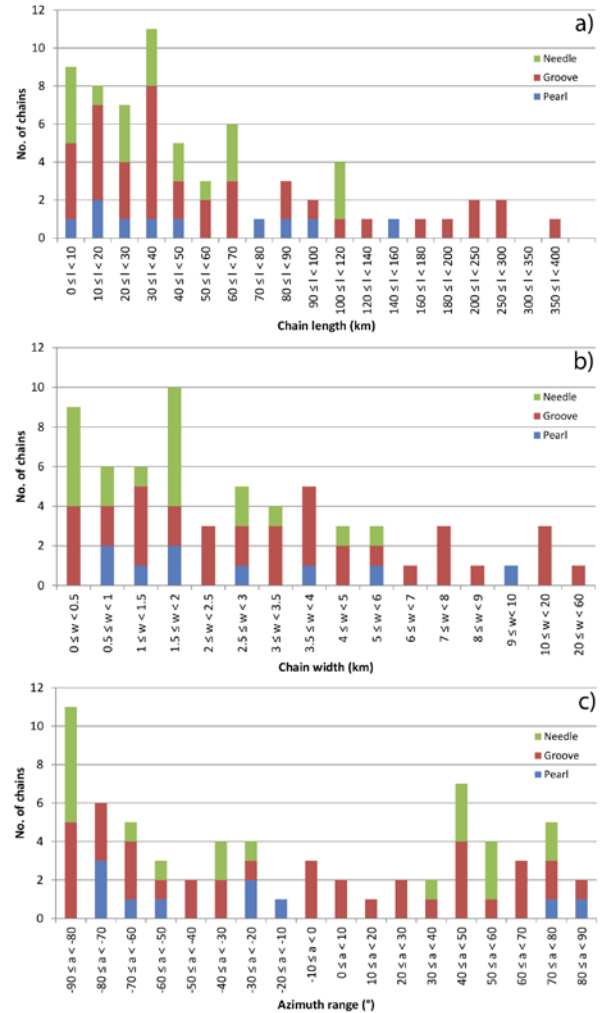


Fig. 3. Histograms of (a) chain length, (b) chain width and (c) chain azimuth for the three chain morphologies.

Table 1. Counts and mean values for chain length, width and positive azimuth for the three chain morphologies.

	Pearls	Grooves	Needles
Count	10	37	19
Length (km)	55	83	43
Width (km)	2.9	5.4	1.7
Azimuth ($^\circ$)	56	50	61

There were no chains recorded at latitudes of greater than 70°N and less than 72°S . The paucity of chains at the northern pole is influenced by the lack of image coverage in that area. 52% of crater chains recorded lie between 105°W and 215°W , 31% of the moon's surface. In order to determine whether the distribution of chains may be influenced by image resolution, we have begun mapping image resolution across Rhea (red

area in Fig. 1). At present we have only mapped the location of coverage better than 0.2 km/px, which is not yet sufficient to state whether image resolution is a factor, but some of the smallest chains have been mapped in very high resolution images (notably at 5°N, 50°W).

Discussion: 80% of the recorded chains are satisfactorily associated with possible source basins and are secondary candidates. Some craters were associated with multiple chains. The crater Fatu (centered at 10°N, 176°W) has five associated chains that are possible secondaries of its impact (see Fig. 4). All five of the chains have small circles that pass through Fatu and the chains lie within 90° of the crater. Aging/dating is subjective on Rhea due to crater saturation and lack of morphological signs of ejecta, but the small circle and scaling law fits of the chains are deemed to be sufficient to regard Fatu as their source crater.

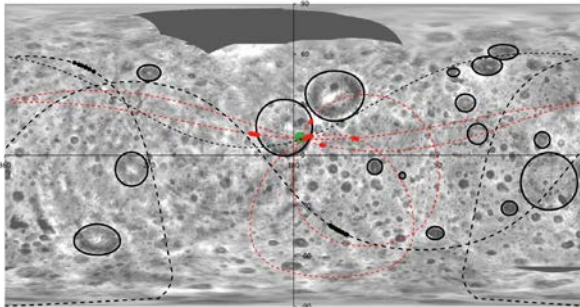


Fig. 4. The five red crater chains display small circle fits (red dashed lines) and sizes consistent with them being secondary chains originating from Fatu crater (in green). The two black chains (with small circles shown as black dashed lines) cannot be linked to any source craters.

Anomalous chains do not have any associated basins that are parental candidates. The black chains in Fig. 4 are anomalous. Neither has a basin within 90° of the proper scaling to be a source. The chain centered at 53°N, 311°W is within the cometary hemisphere while the chain centered at 45°S, 151°W lies in the section of the moon with the most crater chains.

Thebeksan Catenae, an anomalous chain centered at 38°S, 175°W, is by far the largest chain catalogued in terms of area (length of 200 km, width of 54 km), shows a very degraded preservation state and high crater count, and is therefore thought to represent a unique case of a chain formed by a string of large impactors in Rhea's early history.

From Voyager data, Puchou Catenae (33°N, 86°W) was large enough to be designated as a "degraded >500-km-long trough-like structure" [4]. In the present study, it has been classed as an anomalous groove and lies within the cometary hemisphere.

However, due to its proximity and parallel orientation to Wungaran Catenae (18°N, 87°W), both may be of tectonic origin [4].

All the chains identified as being of cometary origin on Ganymede and Callisto lie within a hemisphere that is shifted ~35° towards the leading hemisphere relative to the sub-Jovian point at 0°N, 0°E (i.e. 55°E to 125°W) as a result of the orbital dynamics of the impacting cometary fragments [3]. If it is assumed that cometary impacts on Rhea would be distributed identically, then out of the 13 chains that are cometary candidates, 9 fall within the cometary zone (blue area in Fig. 2). The remaining four may have originated during heavy bombardment early in Rhea's history (in the case of Thebeksan Catenae), or may be endogenic in origin. Significantly, the fact that the majority of the chains considered to be cometary candidates fall within the cometary zone implies that orbital dynamics within the Saturn system do not preclude the fragmentation of comets and their subsequent impact into satellites.

More chains were recorded on Rhea than expected from the study of the Galilean moons. 16 crater chains were identified on Ganymede and Callisto [4], which have surface areas at least an order of magnitude greater, and surface gravities at least 5 times greater, than those on Rhea, and which would therefore be expected to display a much higher chain count. Possible explanations for this discrepancy include imagery of Ganymede and Callisto obtained by Galileo and Voyager being less extensive and of inferior resolution relative to Cassini imagery of Rhea, and the possibility that some chains on Ganymede may have been eliminated through resurfacing.

Future Work: Identification and classification of crater chains on Rhea from the available imagery can be considered complete. The next stage will be to extend this study to the other Saturnian mid-sized icy satellites. This will refine our understanding of the mechanics of secondary, cometary and otherwise anomalous crater chain formation on the icy Saturnian satellites.

References: [1] Shoemaker E. M. (1962) In *Physics and Astronomy of the Moon*, ed. Z. Kopal, 283–359. [2] Oberbeck V. R. and Morrison R. H. (1973) *LPS IV*, pp. 107-123. [3] McKinnon W. B. and Schenk P. M. (1995) *GRL*, 22, 1829-1832. [4] Schenk P. M. et al. (1996) *Icarus*, 121, 249-274. [5] McEwen A. S. and Bierhaus E. B. (2006) *Annu. Rev. Earth Planet. Sci.*, 34, 535-567. [6] Asphaug E. and Benz W. (1996) *Icarus*, 121, 225-248. [7] Allen, C. C. (1979) *GRL*, 6, 51-54.

A QUANTITATIVE APPROACH TO CRATER DEGRADATION ON THE LUNAR SURFACE. M. M. Judson¹ and V. L. Sharpton², ¹State University of New York at Buffalo, Buffalo, NY 14260 (melissaj@buffalo.edu), ²Lunar and Planetary Institute, 3600 Bay Area Blvd, Houston, TX 77058 (vlsharpton@alaska.edu).

Introduction: Accurately assessing the formation age of lunar craters is a critical first step in refining the time-stratigraphic history of the Moon. Crater relative age is typically constrained by two methods: counting superposed craters and measuring ejecta characteristics such as brightness and blockiness.

Crater counts work well for large (complex) craters which have accumulated an adequate number of superposed craters on their floors and ejecta blankets. However, smaller simple craters typically do not contain enough counting area to determine a reliable relative age. Ejecta characteristics have proven useful for subdividing the youngest (i.e., Copernican and Eratosthenian) crater populations; however, ejecta characteristics are obliterated and thus indistinguishable in most older (i.e., Lower Imbrian-Nectaran) craters with diameters (D) ≤ 100 km.

An independent, quantitative means of determining relative ages of small lunar craters would therefore make a significant contribution to reconstructing the stratigraphic history of the Moon.

Objectives: Recognizing that the walls, rim crests, and flanks degrade as a crater ages, we focused our attention on determining the regional slopes characteristics of small ($\sim 2\text{km} < D < 30\text{km}$), fresh (post-mare) lunar craters. Our primary objectives were as follows:

1. constrain the maximum slope magnitude of the inner crater walls and the ejecta-covered flanks;
2. explore the limitations of currently available digital elevation models (DEM) for reliably sampling these slope values;
3. measure how those values change as a function of crater diameter; and,
4. using the selected fresh craters and a small population of significantly older craters, evaluate whether slope characteristics provide a useful means of estimating crater age.

Data and Observations: Data used in this project were retrieved by the Lunar Reconnaissance Orbiter (LRO) and included [1,2]:

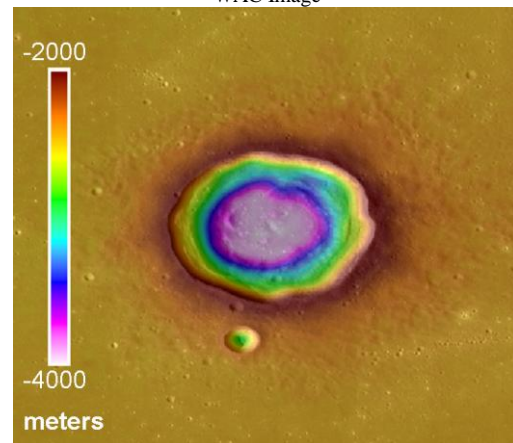
1. images and mosaics from the LRO Wide Angle Camera (WAC) and Narrow Angle Camera (NAC);
2. the global lunar DEM, i.e., WAC_GLD100 (300 m spatial, 20 m vertical resolution) con-

3. structured from LRO WAC stereo images and Lunar Orbiter Laser Altimeter data; and the NAC stereo DEM (2m postings; $\sim 10\text{m}$ vertical resolution) for Linné crater.

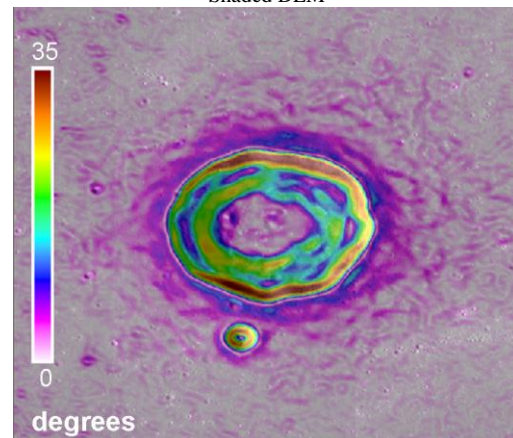
LROC images of post-mare crater Le Verrier:



WAC Image



Shaded DEM



Shaded slope map processed in ArcGIS

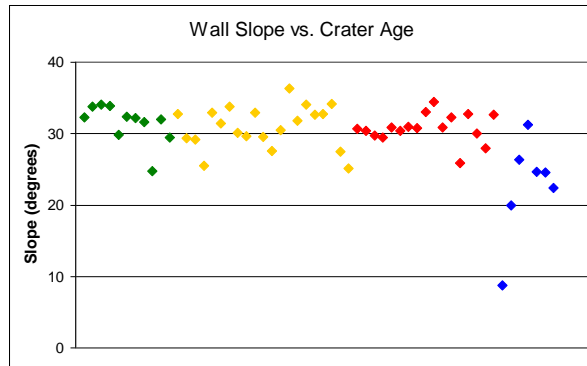


Figure 1

We chose 58 craters to collect data from. Fifty of these were post-mare craters, ranging in diameter from 2.2-20.8 km, and were chosen because of their simple crater form. This size range offers an array of craters with varying characteristics, as craters with 20 km diameters fall into the transition zone between simple bowl-shaped craters and those with more complex morphologies [3]. However, we focused this preliminary study on simple craters to avoid the complications of highly terraced upper wall that typify complex craters. We chose craters superposed on mare surfaces in order to ensure a clear and reliable estimate of the pre-impact surface which is difficult, if not impossible to constrain in highland craters. Furthermore, these craters post-date the emplacement of the mare surfaces and are indisputably very young craters which still retain characteristics that closely approximate the original crater morphology.

All data were ingested in ArcGIS to facilitate analysis. We created a slope magnitude map of the region encompassing all 58 craters using ArcMap's Spatial Analyst toolkit. Slope magnitude, expressed in degrees, was measured over a baseline of ~600 m. For each crater we recorded the maximum slope in sixteen different locations: eight points on the flank and eight corresponding points on the wall of the crater. These values were recorded along with their distance from the rim crest; the eight points for each the wall and flank of the crater were then averaged to produce an "average maximum slope" for each crater.

We then used the LROC ACT-REACT Quickmap to look at the LRO NAC images to get more details on each crater and its ejecta so the degradation state could be estimated independently of the slope data [2]. We measured the size of the continuous ejecta blankets and assessed brightness values and ejecta rays, ejecta block populations, and superposed craters in order to classify craters into one of three groups: Youngest, Middle-aged, and Oldest craters (keeping in mind that all of the craters are very young). Craters classified as youngest

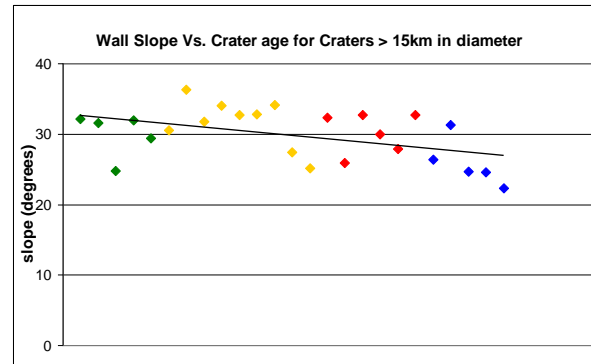


Figure 2

exhibited distinct ejecta rays, abundant blocks, and only a few superposed craters on their upper flanks. Middle-aged craters exhibited either significant ejecta blocks or small ejecta rays and moderate flank craters. The oldest craters showed no ejecta blocks or rays and had flanks that were heavily cratered. We also recorded a separate group of seven pre-mare craters to assess the slope characteristics of craters from a much older time period. Figure 1 shows the average maximum wall slope values for the resulting four age groups: green, yellow, and red symbols signify youngest, intermediate, and oldest post-mare craters, respectively. The pre-mare (oldest) craters are identified by blue symbols. The members of each age (color) group are arranged from smallest to largest. Notice that only the oldest group appears to have a lower average slope than the rest of the groups, and there does not seem to be a steady decline.

Analysis and Conclusions: The reason for the apparent lack of relationship between maximum slope and crater age for smaller craters may be attributed in part to the limitations of the WAC_GLD100 DEM, the best available global elevation model for the Moon [1]. Because smaller craters have narrower crater walls, it is reasonable to expect that the ~600 m baseline slopes derived from this DEM are undersampling the true wall slopes in craters less than some critical diameter.

A clear example of this problem is illustrated with the 2.2 km diameter crater Linné. Using the NAC data (which is not available for all craters/areas of the moon, thus we were not able to use it for all craters) the average maximum wall slope for Linné was found to be 40.1 degrees. Using the WAC_GLD100 DEM we found the average maximum slope for Linné to only be 22.7 degrees [1].

Examining the plot of diameter vs. wall slope (Figure 3), a modest break point occurs at approximately $D=15$ km. Those craters <15 km in diameter (Figure 3A) show virtually no slope dependence on diameter,

suggesting that the actual wall slopes of these craters have been undersampled. However, craters larger than about 15 km (Figure 3B) show a marked size dependence on average maximum slope, suggesting that the undersampling effect is waning with increasing crater size and actual wall slopes are being measured.

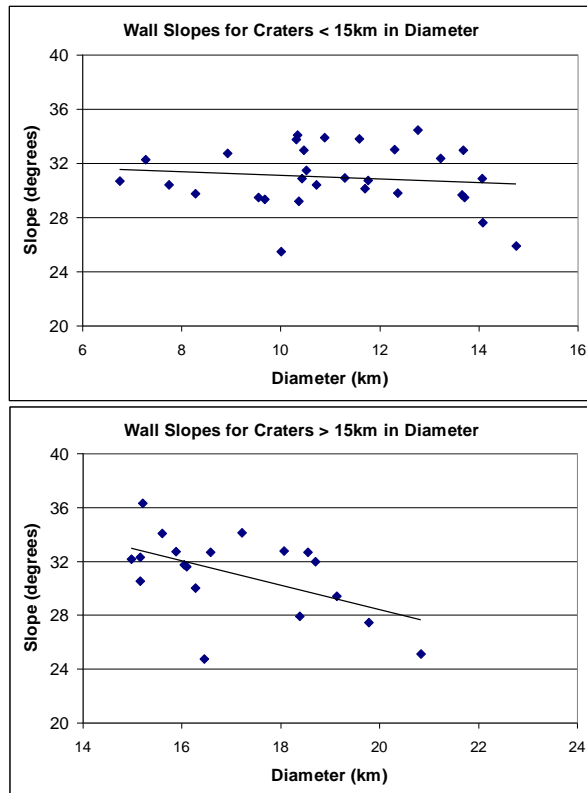


Figure 3: A (top); B (bottom)

Considering that the existing global DEM appears to be inaccurate for craters less than 15 km in diameter, we refined the slope vs. crater age data by removing the craters with diameters less than 15 km. This graph (Figure 2) reveals considerably less scatter in the slope measurements than it did with all the craters included (Figure 1) and also a shallow but significant dip in the age trend that supports the hypothesis that crater wall slopes decline measurably as the crater degrades.

In conclusion, it is apparent that slope constraints are a possible way of assessing crater degradation as a relationship between slope and age was discernible; however, these assessments will not be particularly applicable to research until more high resolution NAC DEMs are obtained. It will be beneficial to study more precise data in the future as more LRO NAC images become available, and observe if the waning slope/degrading crater relationship truly holds. Furthermore, possible extensions of this research would include looking at larger, complex craters, and also

craters located on other areas of the lunar surface, to gain a more wide-ranged and possibly more pertinent slope dataset.

References:

- [1] Lunar Reconnaissance Orbiter Website
<http://www.lroc.asu.edu/>
- [2] LROC ACT-REACT QuickMap
<http://target.lroc.asu.edu/da/qmap.html>
- [3] Pike R. J. (1974) *Geophys. Res. Lett.*, 1, 291-294.

OLIVINE AND SPINEL EXPOSURES AT MOSCOVIENSE AND IMBIRUM BASINS. J.D. Kalynn^{1,2}, G.Y. Kramer² and P.J. McGovern², ¹Department of Earth and Ocean Sciences, University of British Columbia, 6339 Stores Road, Vancouver, BC, V6T 1Z4, Canada, (jessicakalynn@hotmail.com), ²Lunar and Planetary Science Institute, 3600 Bay Area Boulevard, Houston TX, 77058, USA.

Introduction: According to the lunar magma ocean (LMO) theory, the Moon was once a molten ocean that underwent fractional crystallization, resulting in a mafic-rich mantle with a floating plagioclase crust [1]. Under this scenario the mafic mineral olivine is a main component of the lunar mantle, thus any exposures on the surface have been transported there through a geological process such as excavation or volcanism. By investigating the location of these surfaced exposures, we may gain better understanding of the history of lunar geological processes.

Iron-bearing silicates are identified in visible to near-infrared reflectance spectra by absorptions at specific wavelengths resulting from electronic transitions between an iron atom and its surrounding ligands in a crystal structure [2]. The specific wavelength at which maximum absorptions occur are dictated by the composition of a specific mineral, but in general olivine exhibits a broad absorption at 1 μm , spinel a broad absorption at 2 μm , and pyroxene absorptions at both 1 and 2 μm . Recent work with the Kaguya Spectral Profiler (SP) discovered 245 olivine-rich points on the Moon, many of them encircling impact basins [3]. They concluded that some of these detected olivines originated in the upper mantle and were excavated during basin formation. Numerous additional exposures of olivine were found by examining data from the Chandrayaan mission's Moon Mineralogy Mapper (M^3) [4] data; some of these were found to have been transported to the near-surface magmatically [5].

Objective: In this paper we further investigate the olivine exposures at Moscoviense and the northern half of Imbrium (hereafter referred to as Northern Imbrium), on the far side and nearside respectively, using data from the Chandrayaan and Lunar Reconnaissance Orbiter (LRO) missions. These basins on contrasting regions of the Moon, allow us to compare exposures of the mineral with respect to diverse settings (e.g., thick vs. thin crust, pervasive vs. limited volcanism).

The two leading hypotheses on how olivine has come to the surface are the impact transport mechanism, where deep material is brought to the surface during large basin-forming impacts [3,5], and the magmatic ascent mechanism, where intrusive volcanic networks transport melts and cumulates [5]. For the impact transport mechanism we would expect to see olivine exposures along the span of the basin rims, while for the magma transport mechanism we expect to see more localized exposures associated with surface volcanic features.

Methods: M^3 is an imaging spectrometer that has 85 bands between 0.4-3 μm and a spatial resolution of 140 m/pixel [4]. We acquired the level 2 reflectance data which includes photometric, thermal, and ground truth corrections. With M^3 data we identified the spectral signature of olivine. Olivine is identified by its

distinctively wide 1 μm absorption band, made up of three absorption features at 0.85, 1.05, and 1.25 μm , and lack of 2 μm absorption. In order to assist our search we applied an olivine index from the M^3 team that searches for its 1 μm features [6]. To reduce the amount of noisy spectra the index detects from shadows, we applied a mask to eliminate pixels with reflectance values less than 0.05 across all wavelengths.

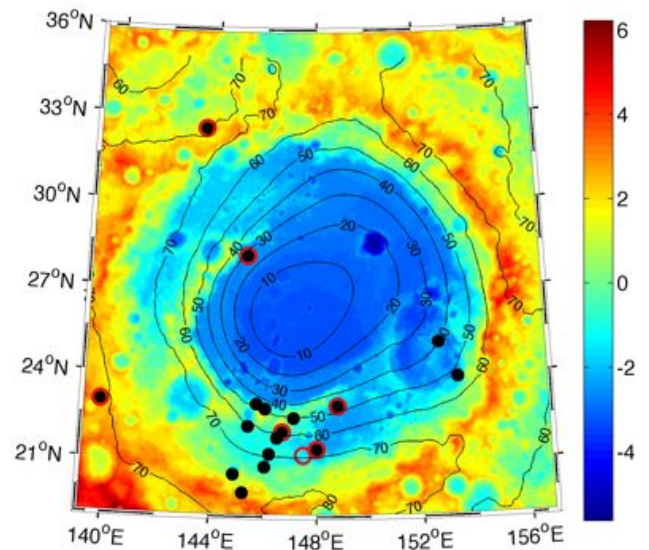


Figure 1 LOLA 512 ppd topography [8] of Moscoviense basin with contours from the Kaguya crustal thickness model [9]. The red circles show the locations of the olivine-rich exposures previously reported by [3]; filled circles indicate those verified with M^3 . The solid black points represent new olivine exposures reported in this paper (Table 1).

In order to determine the geophysical setting of the spectra locations, we utilized the 512 points per degree topography from Lunar Reconnaissance Orbiter's (LRO) Lunar Orbiter Laser Altimeter (LOLA) [7] as well as the crustal thickness model from Kaguya [8]. In addition, we acquired LRO Wide Angle Camera (WAC) images and high-resolution LRO Narrow Angle Camera (NAC) images [9] in order to observe the geological context of the regions.

Observations:

Moscoviense: Following this approach we verified six out of the seven olivine exposures previously discovered with SP [3]. The NAC images show that five of these exposures are associated with small, fresh craters. We report ten more olivine-rich exposures, two at Komarov crater and eight localized in the southwest region of Moscoviense between 19.9 and 23.0°N and between 144.9 and 147.0°E (Fig. 1, Table 1).

The WAC images show that nine of the new olivine detections are also associated with craters. The higher resolution NAC images are only available for four of these outcrops. From these we find no evidence for intrusive or extrusive volcanic structures, such as the dikes seen previously in relation to olivine exposures on the rim of large basins [5], and thus propose these have been transported to the surface by impacts. However we do note that the high proximity of the outcrops in the SW may be characteristics of these olivine exposures originating from a subsurface structure, such as a pluton emplaced at a level of neutral buoyancy [10], a hypothesis that will be able to be tested with data from the Gravity Recovery and Interior Laboratory (GRAIL) mission [11]. We observe no relation between these outcrops and their geophysical setting, elevations at these locations vary between -1.2 and 2.6 km and the estimated crustal thickness beneath them varies between 47.5 and 77.2 km.

Eight of the mineral exposures mapped in Figure 1 show olivine's distinctive spectral signature, while two show the wide $1\ \mu\text{m}$ feature with a minor $2\ \mu\text{m}$ absorption. This may be attributed to the olivine mixing with pyroxene or to Cr-spinel inclusions, which are commonly associated with lunar olivine [12].

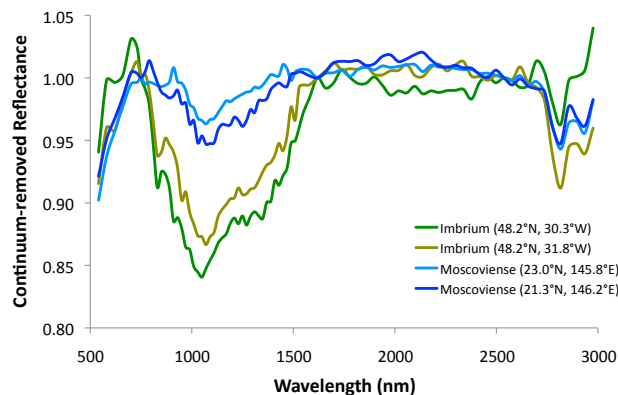


Figure 3 Continuum-removed spectral profiles of olivine exposures at Moscoviense, in turquoise, and at Northern Imbrium, in green.

Northern Imbrium: We identified 19 olivine-rich outcrops (Fig. 2, Table 1) at Northern Imbrium, 4 of the olivine spectra have the minor absorption at $2\ \mu\text{m}$ previously discussed. Six of these exposures lie on the rim and terraces of Plato, a 109 km crater on the northeastern rim of Imbrium. Eleven olivine exposures are located on the northern edge of Sinus Iridum, a 236 km basin, which is manifested as the mountainous rim, Montes Jura. The olivine exposures lie both on the terraces of Sinus Iridum as well as the slumped blocky material. Further, there is one olivine-rich exposure associated with a small km-sized crater on the outside edge of Imbrium's northeastern rim, and one within the Montes Alpes on the inside edge of the northeastern rims.

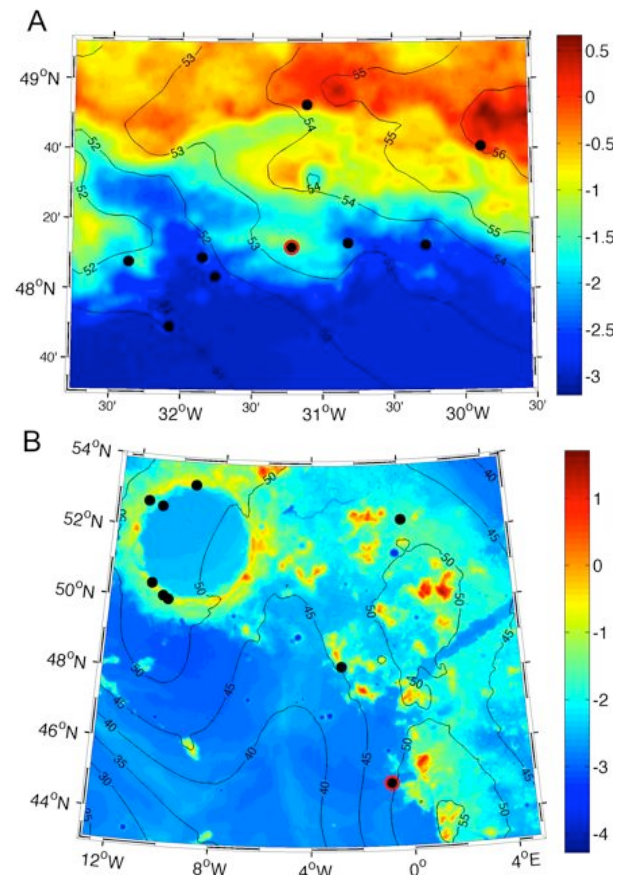
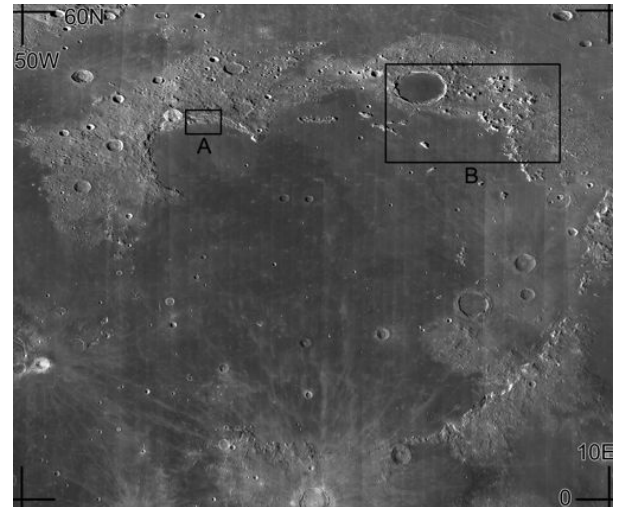


Figure 2 **TOP:** WAC mosaic of Imbrium basin in simple cylindrical projection is context image for topographic figures A and B. LOLA 512 ppd topography of (A) the northern rim of Sinus Iridum and (B) the northeastern rim of Imbrium. The contours and symbols are as in Figure 1.

We did not find any evidence of volcanic activity to support the magmatic transport hypothesis but their locations, spread along the rim of Imbrium and the rims of large craters within, support the impact transport

mechanism. The elevations of the olivine-rich outcrops range between -2.9 and 0.05 km, reflecting the roughness of the terrain at basin and crater rims. The crustal thickness at these points range between 46.0 and 55.9 km, a smaller variance than that seen at Moscoviense basin and consistent with the emplacement over the Imbrium rim region where the crust is thicker.

Spinel at Moscoviense: Exposures of Mg-spinel were first discovered on the Moon in M³ data. The spinel was found in the western region of Moscoviense basin and was claimed to have a possible magmatic intrusion origin [13]. We verified these spinel exposures, and created a spinel index that mimics the algorithm of the preexisting olivine index but looks for a wide 2 μ m feature instead. This resulted in the discovery of several more spinel exposures at Moscoviense, and at different locations including a large region to the NW where the exposures appear to display weak spinel signatures (Figure 4). Due to this signature being more prominent on the sides of the strip that are closest to the Sun, we caution that this needs to be investigated further to ensure this is not an artifact of the photometric and thermal correction.

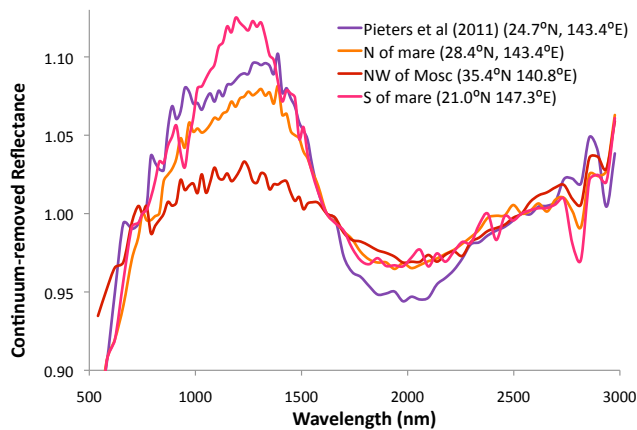


Figure 4 Continuum-removed spectral profile examples of spinel exposures we found at Moscoviense compared to that previously discovered (in purple) [12].

Discussion: While the distinctive signature of olivine is clearly seen in our data, subtle variations in the absorptions at each band create unique spectral profiles. The criteria we are using to characterize the spectra are a) the breadth of the spectral profile and b) the prominence of the 3 absorption features. Figure 3 shows that the olivine outcrops at Northern Imbrium have a broader and deeper 1 μ m absorption than that at Moscoviense. Additionally, the olivine at Moscoviense shows a more prominent 0.85 μ m absorption feature. Variations can be attributed to the composition of the olivine, as its three absorption features discussed are dependant on the Mg content of the exposure. Our preliminary look at the spectra suggest that due to the breadth and shapes of the spectral profiles, the olivine at Northern Imbrium may have a lower Mg content than that at Moscoviense. A more quantitative technique is the Modified Gaussian

Model (MGM), a method that allows one to deconvolve the spectral profile and determine its composition [14]. This method will be useful to apply in the future in order to investigate the variations in our olivine-rich exposures and see if they correlate with their geographical or geological location. Further the composition will help us better understand the origin or transport mechanism of the olivine exposures as primitive mantle sources contain high-Mg olivine, and more evolved sources, such as the upper mantle, contain low-Mg olivine.

We utilized multiple data sets in this paper in our attempt to discover more olivine outcrops and investigate them for evidence of a transport mechanism to the surface (impact [3], volcanism[5]). The distributions and settings of the olivine-rich outcrops reported here favour the impact transport mechanism due to their high association with craters, their independence of local topography and crustal thickness, and the lack of volcanic evidence in the images. As mentioned, we do note that the outcrops in the SW of Moscoviense may have magmatic origins, but due to the fact there are no visible volcanic structures on the surface we suggest the olivine has been transported to the surface by impacts.

Location	Lat (°N)	Lon (°E)	Lat (°N)	Lon (°E)
SW region of Moscoviense	22.2	145.3	23.0 [†]	145.8 [†]
	22.7	146.1	22.3	147.0
	20.9	146.1	21.3	146.2
	19.9 [†]	145.1 [†]	20.6	144.9
Komarov	25.1	152.7	23.9	153.4
Crater E of Plato	52.3 [†]	0.1 [†]		
Rim of Plato	50.1	349.5	50.4 [†]	349.0 [†]
	50.0	349.7	52.8	348.5
	52.6*	349.1*	53.2 [†]	350.6 [†]
Mont.Alpes	48.2*	357.3*		
North rim of Sinus Iridum	48.1*	329.2*	48.1	328.3
	48.9	328.9	48.1	327.6
	47.8	327.9	48.2	328.2
	48.2 [†]	329.7 [†]	48.7	330.1

Table 1 The location of the new 26 olivine-rich exposures reported in this paper; excludes those in Table S1 of [3]. [†] identifies the exposures that also have a minor 2 μ m absorption, and * identifies outcrops that may correspond to those shown in Figure 2 and not listed in Table S1 of [3]

References: [1] Snyder, G.A., et al (1992) *Geochim. Cosmochim. Acta*, 56, 3809-3823. [2] Burns, R.G. (1993) *Cambridge Univ. Press*. [3] Yamamoto, S., et al (2010) *Nat. Geosci.*, 3, 533-536. [4] Pieters, C.M., et al (2009) *Curr. Sci.*, 96(4), 500-505. [5] Powell, K.E., et al (2012) *LPSC*, 43, 1689. [6] Nettles, J., *Personal Communication*. [7] Smith, D. E. et al., 2010. *Geophys. Res. Lett.*, 37, L18204. [8] Ishihara, Y., et al (2009) *Geophys. Res. Lett.*, 36, L19202. [9] Robinson, M.S., et al (2010) *Space Sci. Rev.*, 150, 81-124. [10] Head, J. W. III and Wilson, L. (1992), *Geochim. et Cosmochim. Acta*, 56, 2155. [11] Zuber, M.T. et al (2008) *LPSC*, 39, 1074. [12] Isaacson, P.J., et al (2011) *Jour. Geophys. Res.*, 116, E00G11. [13] Pieters, C.M., et al (2011) *Jour. Geophys. Res.*, 116, E00G08. [14] Isaacson, P.J. and C.M. Pieters (2010) *Icarus*, 210, 8-13.

THE GALE CRATER MOUND IN A REGIONAL GEOLOGIC SETTING: MAPPING AND PROBING SURROUNDING OUTCROPS FOR AREAS AKIN TO THE CENTRAL MOUND AT GALE. L. Korn¹ and C. Allen², ¹Department of Geosciences, University of Massachusetts Amherst, Amherst, MA 01003 (slbkm12@yahoo.com), ²Astromaterials Research and Exploration Science, NASA-JSC (carlton.c.allen@nasa.gov).

In this project we search for areas within a 1,000km radius of Gale Crater that match the upper and lower parts of the central mound in terms of altimetry, geology, age, and thermal inertia.

Introduction: There are currently several hypotheses on the origin and ubiquity of the deposited sequences in the central mound at Gale Crater on Mars. The hypotheses range from aeolian ice or volcanic deposits [1, 2, 3], lacustrine deposits [1, 2, 3], hydrothermal spring deposits [1, 2, 3], ground water upwelling and evaporation [1], and ancient polar deposits [2]. However, because there are no unambiguous volcanic landforms such as vents or flows, the sequences are likely sedimentary [2].

The Mars Science Laboratory's Rover Curiosity has been targeted to land in the flat, northwestern area inside the crater on August 6th, 2012 and it will begin its 2 year expedition at Gale [4]. Curiosity will be analyzing samples and taking photographs along its traverse towards the central mound. Here, it will begin its ascent through a channel [1] centered within an outcrop of white yardangs, an area that may potentially provide insight into former fluvial activity at Gale [4].

Gale is a 155km diameter crater that was formed in the Late Noachian or Early Hesperian epoch. The crater is situated along the Dichotomy, which divides the smooth Northern Lowlands from the rough, highly cratered Southern Highlands. The boundary is distinguished by fretted terrain, lobate debris aprons, and lineated valley fill [5]. The Dichotomy was perhaps created by an impact [6, 7], a change in crustal thickness [6], glacial retreat and/or formation [5], volcanic activity [7], tectonic activity [7, 8, 9], or a combination of processes. Still, some of it is buried under volcanic debris and other rises [7] making it difficult to determine the Dichotomy's exact breadth.

Located at 5.3S and 137.7E, Gale is distinct in its situation along the Dichotomy as well as its conspicuous central mound. The mound sits at the center of Gale and rises 5.2km up from the crater floor [1]. It is divided into an upper (UM) and a lower mound (LM) which are separated by an erosional unconformity [2]. The geologic sequences in the LM seem to span the Late Noachian/Early Hesperian epoch, a time when Mars's climate transitioned from warm and wet to cool and dry [4]. The age of the UM is poorly constrained, but it is generally considered younger than the LM based on superposition.

The LM is characterized by parallel beds and yardangs of varying thickness, albedo, texture, and dip angle [2]. The UM is composed of finer layers at higher angles [1]. Additionally, the UM contains an array of features including yardangs, fine layers, mountainous features, lobate features, and serrated erosional patterns [3]. Moreover, the LM demonstrates an upward progression of phyllosilicate to sulfate rich sediments [4], contrasting the UM's complete lack of such hydrated minerals [4].

The upper-most portion of the central mound rises above the northern section of the crater rim that flanks the Northern Lowlands, but it is at the same height or lower than the southern rim. This distinction causes many to speculate whether or not the crater was potentially subjected to an influx of fluvial or lacustrine deposits at one time [1-4, 10- 12]. Parker [12] suggests that the Northern Lowlands were either partially or entirely filled with water, and much of the LM could have been formed in that environment.

Procedures: In this study, we use orbital remote sensing data to determine if areas within a 1,000km radius of Gale Crater have similar characteristics to Gale's central mound. Maps were constructed from

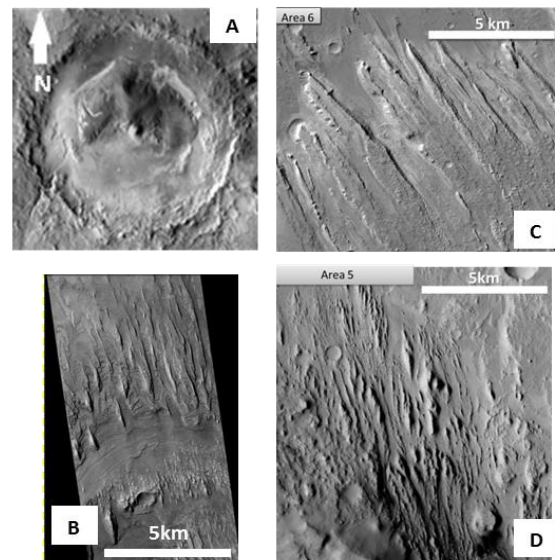


Figure 1: *Image A:* Gale Crater in THEMIS Daytime Infrared. *Image B:* The Eastern Lower Mound at Gale (HiRISE:ESP_01965_1745). *Image C:* Area 6 (CTX: B21_017799_1765). *Image D:* Area 5 (CTX: P05_002899_1759). *Images C and D* are analogues to *Image B*, in terms of altimetry, age, brightness (a proxy for thermal inertia) and geology. All images except *Image A* are at the same scale.

Table 1: List of Geologic Units from Thompson et al. (2011)

UNIT	NAME	ELEVATION	BRIGHTNESS
LML	Lower Mound Eastern Layered Unit	-1500m to -3250m	50-175
UML1-2	Upper Mound Subdued Layers 1-2	300m to -1350m	0-175
UMP	Upper Mound Mountainous Unit	300m to -2100m	0-175
UMC	Upper Mound Chaotic Unit	-1800m to -2900m	100-200
UME3	Upper Mound Etched Unit 3	-1850m to -3200m	100-150

The above table shows the geologic units used in the specific study. Elevation is taken from MOLA Altimetry and brightness from THEMIS Nighttime Infrared. Units and names come from the Thompson et al. (2011) map [1].

day and night infrared images obtained by the Thermal Emission Imaging System (THEMIS) on the Mars Odyssey spacecraft, images from the Mars Orbital Camera (MOC) and altitude data from the Mars Orbiter Laser Altimeter (MOLA) on Mars Global Surveyor, and Context Camera (CTX) and High Resolution Imaging Science Experiment (HiRISE) images from the Mars Reconnaissance Orbiter.

A base map encompassing a 1,000km radius circle around Gale Crater was constructed in ArcGIS using the THEMIS Daytime Infrared Mosaic. A geographic information system (GIS) layer was defined by the upper and lower altitudes of Gale mound (-4,600m to about 400m). A second layer was defined by geologic units from the U.S. Geologic Survey Mars Global Geologic Map I-1802-B that spanned the Late Noachian/Early Hesperian time boundary. A third layer was defined by the brightness value range for the Gale mound as seen in the THEMIS Nighttime Infrared Mosaic (0-250). These brightness values are correlated with near-surface thermal inertia.

These layers in ArcGIS were combined to define regions of interest that match the Gale mound in terms of altitude, age, and brightness (a proxy for thermal inertia). HiRISE, MOC, and CTX images pertaining to these regions were then collected and explored in order to find specific areas with geologic features analogous

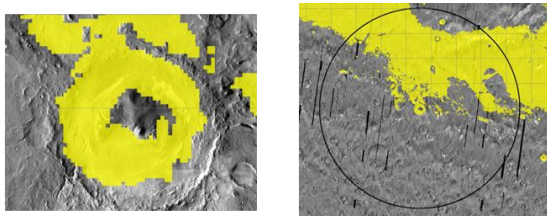


Figure 2: The above images show THEMIS Daytime Infrared overlain by MOLA Altimetry. Gale Crater with a 155km diameter is on the *LEFT*. The 1000km radius circle surrounding Gale is on the *RIGHT*. Both Images show areas below an altitude of -2300m.

to those in the central mound (Fig. 1). Explicit comparisons were developed using the geomorphic units mapped by Thompson et al. [1]. The units used for this study can be found in Table 1.

Additionally, a map was created using MOLA altimetry in order to demonstrate the altitude correlation between the Northern Lowlands and the crater (Fig. 2). This map delineates altitudes that are below -2,300m, a possible “base level” defined by channel morphology in Gale [11].

Lastly, craters of analogous size to Gale were studied and imaged using GoogleMars (mars.google.com) and the THEMIS Daytime Infrared Mosaic. The sizes of the selected craters ranged from 140km to 169km in diameter and the study covered the entirety of Mars.

Results: Based on the regional study, areas of similar age, brightness (a proxy for thermal inertia), and altimetry as the central mound can be found northwest and southeast of Gale. These areas are more or less directly on or along the Dichotomy. Areas matching the LM’s altitude range of -2,250m to roughly -4,050m, and THEMIS Nighttime Infrared brightness range of 50 to about 250, were found in the Npl2 unit to the southeast. UM analogues within an altitude range of 400m to -3,200m, and a THEMIS Nighttime Infrared brightness range of 0 to 150, were found in the HNu unit to the northwest. The Npl2 unit is Late Noachian in age, with subdued or partially buried craters and crater rims as well as thin lava flows and sedimentary deposits [13]. The HNu unit is Mid-Noachian/Mid to Early Hesperian in age and consists of undivided material representing crater remnants and partial plateaus [13].

For the specific study within the established regional areas, it was determined that analogues to the LM were found roughly 230km southeast of Gale. Areas 5 and 6, with altitude ranges spanning -2,850m to -3,050m and -2,000m to -2,650m, respectively, as well as THEMIS Nighttime Infrared brightness ranges of 125 to 200 and 75 to 200, respectively, matched the LML unit (Table 1). These areas also matched the LML in geomorphology, containing yardangs and slight layering (Fig. 1).

The UM analogues were found to the northwest and southeast of Gale. These areas include altitude and THEMIS Nighttime Infrared brightness ranges of roughly -200m to -2,350m and 50 to 200 for UML1-2, 250m to -2,150m and 75 to 175 for UMP, -1,400m to about -2,550m and 50 to 200 for UMC, and -2,400m to -2,500m and 100 to 225 for UME3 (Table 1). These UM analogues were found between 260km and 900km northwest of Gale, except the UME3 area, which was 440km southeast of Gale. These analogues matched

the UM in terms of yardangs, layers, serrated erosional patterns, and mountainous features.

For the last two aspects of the study, it was found that MOLA altimetry, between -4,600m to -2,300m, covered the northwestern portion of the crater (Fig. 2). This range enclosed the entire LM, terminating near the unconformity situated beneath the high albedo yardangs of the UM, and above the western lobe of the LM. Additionally, this range enveloped a 500m-wide channel along the northern rim of the crater, an area in direct contact with the Northern Lowlands and the LM analogues to the southeast (Fig. 2).

Lastly it was established that craters of similar size to Gale have central peaks, remnants of peak rings, or were too eroded or filled to see any central features (Fig. 3). No crater in the study contained a central mound or feature akin to the central mound at Gale. However, it should be noted that most craters in question are either full of sediment, or show signs of erosion and additional cratering, potentially obstructing or destroying any central features.

Discussion: Gale is one of a large number of Martian craters that have been partially or completely filled with sediments, likely kilometers thick. In some large craters, a portion of this sediment has been removed. An analogous process at Gale could have produced an eroded crater and a central mound composed of sediments that are related to sediments found outside of the crater.

There are several analogues for both the UM and LM units at Gale that have the same altimetry, THEMIS Nighttime Infrared brightness, age and geology. The analogues for the LM are found in a Late Noachian geologic unit. The LM areas also have similar geomorphological features such as yardangs and layers, though the features may not look identical to those of the LM. These discrepancies may be attributed to the fact that the central mound is within a crater and these analogues are found as outcrops separate from surrounding mesas, or between large channel features.

Some of the UM analogues are found in a Late Noachian geologic unit, but most are located in a Mid to Early Hesperian unit. These outcrops contain a plethora of features including mesas, channels, erosional features, and mound remnants. As of yet, no areas were found that match the highest portion of the UM. However, areas were found that had layers, yardangs, and erosional patterns nearly identical to the majority of the UM features. Considering that the regional study and specific study found the LM and UM analogues within the HNu and Npl2 units, respectively, we can conclude that the LM areas are older than the UM areas, though the exact age

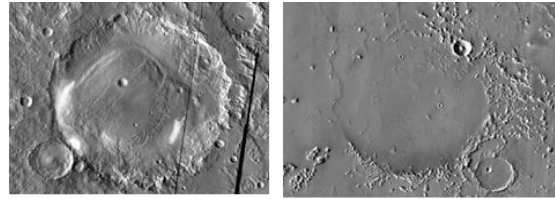


Figure 3: The above images depict craters that are similar in size to Gale. The *LEFT* crater has a diameter of 168km and is filled, eroded, and cratered. The *RIGHT* crater has a diameter of 140km and it is completely filled. Images are from THEMIS Daytime Infrared Mosaic.

difference cannot be presently determined based on available data.

The map showing areas below -2,300m illustrates that both Gale and the adjacent Northern Lowlands could have been flooded if water ever reached that level. Channels that cut into the mound and in the southern rim of Gale suggest potential flooding at this altitude, and channels in the northern rim of Gale suggest potential flow between the crater and the Northern Lowlands. Additionally, areas in the Lowlands with similar morphology to the lower mound are seen at approximately this level. These observations could potentially correspond with the current hypothesis that either all or part of the lower mound was formed underwater.

Conclusion: We have found areas within a 1,000km radius of Gale Crater that are analogous to the upper and lower components of the central mound at Gale. These results are consistent with a model of the geologic history of Gale that includes the deposition of potentially kilometers of sediment, possibly in a lacustrine environment, followed by large scale erosion and more deposition, which left behind the unique central mound that we see today.

References: [1] Thompson et al. (2011) *Icarus*, 214, 413-432. [2] Milliken et al. (2010) *GRL*, 37, L040201. [3] Anderson, Bell (2010) *Mars*, 5, 76-128. [4] Andrews-Hanna et al. (2012) 3rd Conference on Early Mars, Abs, 7038. [5] Head et al. (2006) *GRL*, 33, L08S03. [6] Andrews-Hanna et al. (2008) *Nature*, 453, 1212-1216. [7] Milbury et al. (2007) *Planet. Space Sci.*, 55, 280-288. [8] Andrews-Hanna et al. (2012) LPSC XLIII, Abs, 2706. [9] Lendaric et al. (2004) *JGR*, 109, E02003. [10] Edgett et al. (2008) 3rd MSL Landing Site Workshop. [11] Sumner et al (2011) 5th MSL Landing Site Workshop. [12] Parker (2010) 5th MSL Landing Site Workshop. [13] Greeley, Guest (1987) *USGS*, I-1802-B.

Composition Analysis of the Marius Hills Volcanic Complex Using Diviner Lunar Radiometer Experiment and Moon Mineralogy Mapper. K. M. Lehman^{1,2}, G. Y. Kramer², W. S. Kiefer², ¹Texas Christian University, School of Geology, Energy, and the Environment, Fort Worth, TX, ²Lunar and Planetary Institute, Houston, TX.

Introduction

The Marius Hills Volcanic Complex, located in Central Oceanus Procellarum at 13.3 N, 306.8 E, has an undoubtedly complicated volcanic history. Over 250 domes and complicated surrounding volcanic geomorphologies suggest multiple volcanic episodes [1]. In light of this, many have investigated potential compositional differences using both Clementine and Chandryann-1's Moon Mineralogy Mapper (M³) and have identified the area as a high titanium basalt with glass features surrounding cones, associated with pyroclastics [2,3,4]. Beyond subtle variation in FeO percent, TiO₂ percent and olivine content, though, the complex has been deemed compositionally homogeneous [2,3,5]. Recent geophysical research has shown a large gravity anomaly under the Marius Hills complex that can be best explained by a large magma chamber, large enough to allow for significant magma evolution [6]. This new evidence made it important to analyze possible compositional differences using data sets that have not been used before.

Our study makes use of two complementary spectral datasets. M³ is an imaging reflectance spectrometer that can detect 85 channels between 460 to 3000 nm, and has a spatial resolution of 140 meter per pixel [7]. M³ can determine mineralogy in reflectance spectra through diagnostic absorptions at specific wavelengths, which result from electronic transitions between an iron atom and its surrounding oxygens in a crystal structure [8]. The specific wavelengths at which these absorptions occur are dictated by the composition and crystal structure of a specific mineral. Previous analysis of the near infrared spectrum of the Marius Hills used a preliminary calibration of M³ spectroscopy [5], whereas our analysis uses the final calibration of the M³ dataset.

The Lunar Reconnaissance Orbiter's (LRO) Diviner Lunar Radiometer Experiment has a spatial resolution 950 m/pixel [10] produces thermal emissivity data and can provide compositional information from 3 wavelengths centered around 8 microns that are used to characterize the Christiansen Feature (CF) [9, 10]. Each CF value is indicative of a certain silicate mineral composition, with higher values being a more mafic material and lower values being felsic [9, 10]. This feature is not affected by vitrification and the value can be assumed to be based on linear mixing of the material [9, 10]. It is also important to note that a low CF value has a high correlation to high visual albedo, and that space weathering causes the CF value to move to longer wavelengths [10, 11]. All this makes the CF

value very helpful in understanding the geology of an area. This value is complementary to M³ spectra, allowing for more felsic materials to be observed and for a deeper understanding of the entire compositional mixture as comparison between spectra compositions and Diviner compositions occur.

Methodology

Three different data sets were used to analyze this region: Clementine, M³ spectral data, and the Gridded Level 3 Diviner Christiansen Feature map.

We initially used RGB (Band-Ratio Color Composite) [12], TiO₂ [13], FeO [14] spectral image maps from the 5 channel UV VIS imager on the Clementine spacecraft. We also used M³ data to create spectral parameter maps, that were designed to highlight regions that are rich in particular materials such as olivine and high calcium pyroxene. The M³ maps were overlaid on to the Clementine data to differentiate chemically different areas. These areas were then analyzed using the M³ spectral profiles to see if there were actual notable changes in the spectra. We particularly focused on looking for possible spectral differences between the Marius Hills volcanic domes and the lava plains between the domes. Based on the geologic regions mapped out using these parameters we extracted representative M³ spectra for more detailed spectral analysis.

We also looked for possible differences in the location of Christiansen absorption frequency using Diviner radiometer results [9, 10]. Areas that displayed differences were then compared with their M³ spectral counterparts to see if there was a correlation between the two data sets. Finally, Lunar Reconnaissance Orbiter Camera (LROC) and WAC GLD 100 stereo topography model were used to try to understand the geomorphology of the areas that appeared chemically different.

M³ Analysis

The new analysis of the Marius Hills complex using the most recent M³ calibration bears similar results to previous studies. The complex appears relatively homogeneous spectrally, with variations only seen in the absorption band depths and the reddening (maturity) of the spectra. As seen in Figure 1, the spectra display classic pyroxene absorptions, primarily that of clinopyroxene, with its 1 and 2 micron absorptions shifted to longer wavelengths [15]. Previous studies had described an olivine rich flow within the complex [5], but we did not see this variation using the most

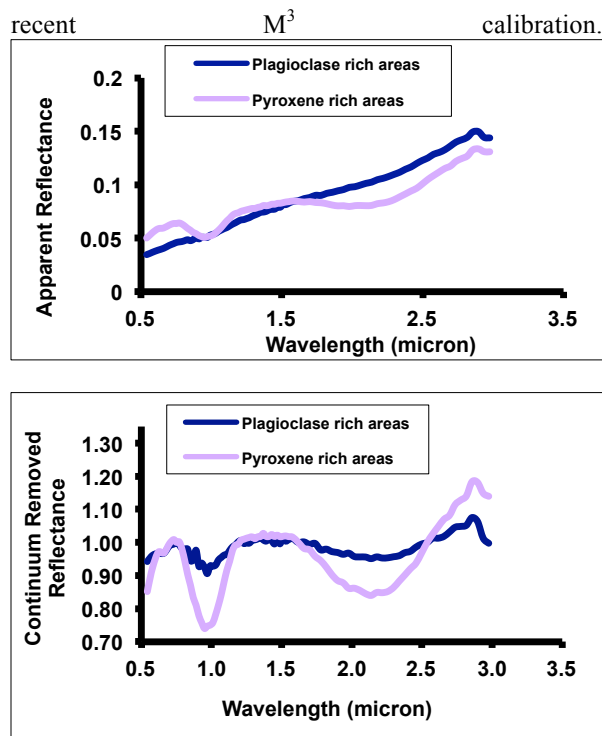


Figure 1: These graph displays the difference between the Plagioclase rich areas (purple) and the surrounding non plagioclase rich areas (blue). Top: Raw spectra Bottom: Continuum Removed spectra. Removing the continuum slope from the top spectra emphasizes the relative strength of the 1 and 2 micron absorptions for pyroxene. As can be seen, the Plagioclase rich areas are brighter with muted absorptions.

Diviner Analysis

Previous studies have used Diviner data to map more silica rich areas on the moon, but none of these have focused on the Marius Hills Complex [9, 10]. Although the area had an average CF value of 8.3 microns suggesting a pyroxene rich substance, there are areas across the complex that have CF values ranging 7.9- 8.2 microns suggesting a more plagioclase rich area. These plagioclase regions are associated with many craters, rilles, possible volcanic vents and with 8 large domes. The largest of these lower CF value domes is made up of 65 diviner pixels covering approximately 62 km². For each roughly km sized pixel, the CF value, and thus the composition, can be assumed to be based on linear mixing of the constituent minerals. For example, a CF value of An₉₄₋₉₆ plagioclase is 7.9 microns. Therefore these km-sized areas with CF between 7.9 and 8.2 microns contain either a plagioclase- rich basalt for the whole region or contain concentrated regions of exposed plagioclase surrounded by more mafic minerals [10].

These areas when compared to Clementine RGB and TiO₂ parameters are shown to be surrounded by higher Ti materials. When spectrally analyzed using M³ data, these plagioclase rich areas displayed

muted pyroxene absorptions and a brightening of the spectra.

Discussion

The new Diviner data shows what M³ could not alone, plagioclase rich regions in the Marius Hills complex. Mineral components that combine to form reflectance spectra do not mix linearly at modal abundances as low as 10 percent strongly absorbing dark minerals, such as olivine, pyroxene, ilmenite, can overwhelm and obscure a plagioclase spectrum [10]. Bright craters and bright areas surrounding domes in the NAC images which are associated with low CF values are assumed to be the plagioclase-rich areas. These bright, plagioclase rich areas, are often surrounded by very low albedo which may be more ilmenite rich materials.

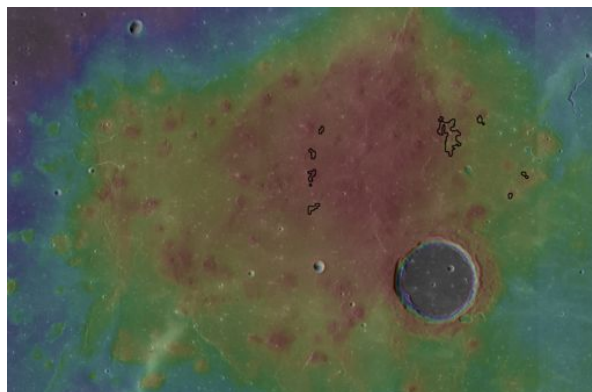
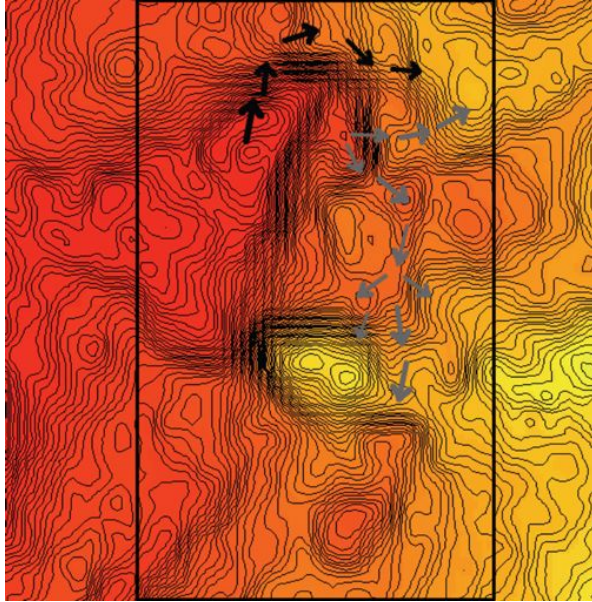


Figure 2: This map, which has a WAC image overlaid by a color relief map based on WAC GLD 100 topography as its base, displays the plagioclase rich domes. The 8 major domes that are observed as plagioclase rich by the Diviner Lunar Radiometer Experiment are outlined in heavy black.

Remote sensing observations show that the Marius Hills basalts are relatively high in Ti [17]. Based on this, we use Apollo 17 high titanium basalt 70215 as an analog for the crystallization of the Marius Hills basalts. Petrographic observations and experimental crystallization studies show that the major minerals in 70215 began crystallizing in the following order: olivine, ilmenite, and then pyroxene and plagioclase appeared nearly simultaneously near 1150 °C [16]. With further cooling, olivine reacts with the residual liquid to produce additional clinopyroxene. Recent gravity mapping revealed the presence of a large gravity anomaly beneath the Marius Hills that may be due to the presence of a solidified magma chamber [6] and which would provide a location for magmatic evolution to occur by separation of crystals and residual liquid. If the separation of crystals and magma occurred near 1150 °C, the residual magma would be enriched in plagioclase and depleted in olivine and ilmenite relative to the starting composition. Moreover,



by removing olivine from the system before it fully reacted with the liquid to form pyroxene, the final crystallization product of the residual liquid would also be depleted in pyroxene relative to the original source material. These characteristics are consistent with the spectral characteristics of the bright material identified in this study. The dark material that surrounds the bright flows might be the pyroxene-, olivine-, and ilmenite-rich material that is complementary to the plagioclase-rich flows. We therefore propose that our spectral observations are evidence for magma evolution within the Marius Hills magma chamber.

Conclusion

By examining the Marius Hills complex using calibrated M^3 data and Diviner CF value map, three important conclusions were made. First, the M^3 spectra showed that the complex was relatively compositionally homogenous, supporting earlier observations. Second, the olivine-rich basalts previously observed [5] in the complex were not seen in the more recent M^3 calibration nor the Diviner data. Finally, Diviner data made plagioclase rich areas observable, suggestive of magma evolution of the large magma chamber observed geophysically.

References:

- [1] J.L. Whitford-Stark and J.W. Head (1977) Proc. Lun. Plan. Sci. Conf. 8, 2705-2724
- [2] C.M. Weitz and J.W. Head (1999) JGR:104, 18933-18956
- [3] D. J. Heather, S. K. Dunkin, L. Wilson (2003) JGR:108.
- [4] Prettyman et al., JGR 111
- [5] S. Besse et al. (2011) JGR: 116.
- [6] W. S. Kiefer. JGR in review
- [7] C.M. Pieters et al. (2009) Curr. Sci. 96(4), 500-505.
- [8] R. G. Burns (1993) Camb. Univ. Press, 551
- [9] T. D. Glotch et al. (2010) Sci. 329, 1510
- [10] B. T. Greenhagen et al. (2010) Sci. 329, 1507
- [11] P. J. Lucey et al. (2010) Proc. Lun. Plan. Sci. Conf. 41, 1600
- [12] C. M. Pieters (1983) JGR 88, 9534-9544
- [13] A. S. McEwen (1994) Sci. 266, 1858-162
- [14] P. G. Lucey et al. (2000) JGR 105, 20297-20305
- [15] B. B. Wilcox et al (2005) JGR 110
- [16] R. L. Klima et al. (2011) Met. Plan. Sci. 46, 379- 39
- [17] J. Longhi et al. (1974) Proc. Lun. Conf. 5447-5469.

Figure 4: Here, the largest plagioclase-rich dome has CF values as low as 7.96 microns. **Top:** The base map is a WAC GLD 100 topographic map with contours every 10 m elevation change. Two flow movements are described with arrows having different shades of gray. This flow movement is based on the pattern of the increasing CF value coincident with the decrease in elevation. **Black box** shows bounds of bottom figure. **Bottom:** NAC mosaic context image (width is 10 km).

METAL-SILICATE PARTITIONING OF Bi, In, AND Cd AS A FUNCTION OF TEMPERATURE AND MELT COMPOSITION. N. Marin¹, K. Righter², L. Daniieldson², K. Pando², C. Lee³ ¹School of Earth and Space Exploration, Arizona State University, Tempe, AZ 85287 (Nicole.marin@asu.edu) ²Johnson Space Center, Houston, TX 77058 ³Department of Earth Science, Rice University, Houston, TX 77005

Introduction: The origin of volatile elements in the Earth, Moon and Mars is not known; however, several theories have been proposed based on volatile elements such as In, As, Se, Te and Zn which are in lower concentration in the Earth, Moon, and Mars than in chondrites. Explanations for these low concentrations are based on two contrasting theories for the origin of Earth: equilibrium core formation versus late accretion. One idea is that the volatiles were added during growth of the planets and Moon, and then mobilized into the metallic core (e.g., [1]). The competing idea is that they were added to the mantles after core formation had completed (e.g., [2]). Testing these ideas involves quantitative modeling which can only be performed after data is obtained on the systematic partitioning behavior of volatile elements with temperature, pressure and melt composition. Until now, such data for Bi, In, and Cd has been lacking. After conducting a series of high pressure, high temperature experiments in this study, the metal-silicate partition coefficients of Bi, In, and Cd as a function of temperature and melt composition can be used to evaluate potential conditions under which terrestrial planets differentiated into core and mantle, and how they acquired volatiles.

Procedure: Experiments were conducted at constant pressure and variable temperatures using a non-end-loaded piston cylinder apparatus with a Type C W-Re thermocouple at NASA-JSC. The sample used for these experiments was a ground, mechanically mixed powder composed of 70 wt. % Knippa basalt, the composition of which is described in [3], 24 wt. % Fe, and 2 wt. % each Bi₂O₃, In₂O₃: SnO₂ (90:10 wt %), and Cd. Polycrystalline MgO, and graphite were the two capsule types used in an assembly with a BaCO₃ pressure medium. Upon reaching a constant pressure of 1.0 GPa, samples were heated to silicate superliquidus temperatures for durations based on equilibration times from previous experiments ([4], [5]). Afterwards, the samples were power

quenched to glass or polyphase quench crystals surrounding large metallic liquid spheres. Three different experiment series were performed including a time series with graphite capsules, and two temperature series from 1500 to 1900°C, each using different capsules (either MgO or graphite) for a total of 14 experiments.

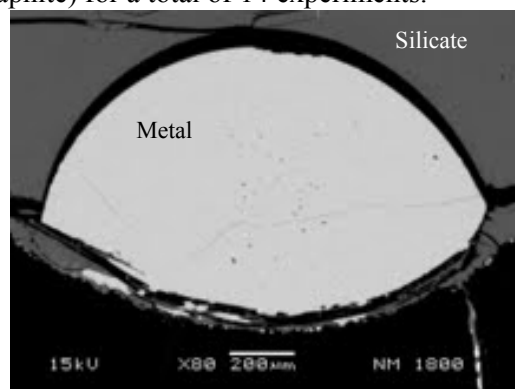


Fig. 1. Back scattered electron (BSE) image of sample NM-1800 run at 1800°C for 15 min. The sample resulted in quenched metallic liquid (lightgray) surrounded by silicate glass (dark gray) which is encased in the graphite capsule (black)

Analysis: Figure 1 is a back scattered electron (BSE) image from the scanning electron microscope (SEM) of sample NM1800. The bright phases are spheres of metal that equilibrated with the silicate melt which is darker. For experiments carried out with graphite capsules, all metals were carbon saturated. The metal and silicate samples were analyzed for major element composition using a Cameca SX100 for electron microprobe analysis (EMPA) at NASA-JSC. A 1 µm beam was used at 20kV and 10nA. Also, a variety of natural and synthetic standards were used. In each sample, the Bi, In, and Cd content of the glass was lower than the detection limit of the EMPA; therefore, the samples were analyzed for trace element composition using Laser Ablation Inductively Coupled Mass Spectrometer (LA-ICP-MS) at Rice University [1]. Standards used for the laser analysis were NIST610, NIST612, BHVO2g, and BCR2g glasses. Analysis was per-

formed at Low Resolution (LR) and normalized to ^{43}Ca isotope. The only trace elements specifically studied for this research were ^{42}Ca , ^{43}Ca , ^{111}Cd , ^{110}Cd , ^{115}In , ^{117}Sn , ^{118}Sn , ^{119}Sn , ^{209}Bi , ^{69}Ga , and ^{71}Ga . Data from the analysis of ^{209}Bi , ^{111}Cd , and ^{115}In at LR was used to calculate Cd, In and Bi in ppm in the silicates. By the abstract deadline, analysis is only complete for the MgO capsule experiments.

Results and Discussion: The trends in figures 2, 3 and 4 (see also, table 1) are showing that the equilibrium model for core formation is possible if the conditions under which the core formed were around 3000 C. Further experiments would need to be conducted at higher temperatures to adequately test this hypothesis.

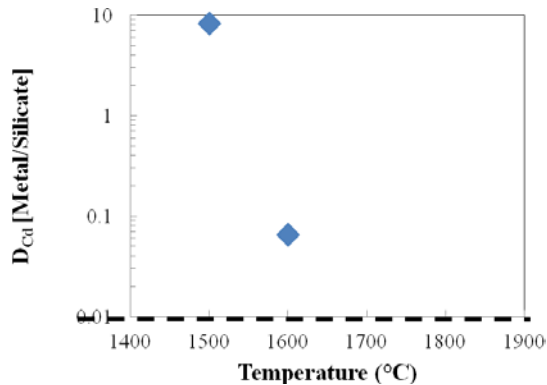


Fig.2. Partition coefficients with respect to temperature for Cd. The dashed line is the D_{Cd} required for core-mantle equilibrium in the Earth.

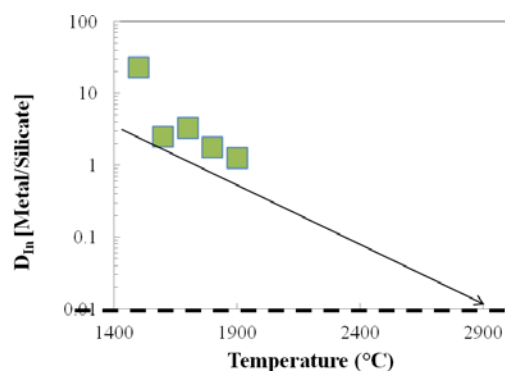


Fig.3. Partition coefficients with respect to temperature for In. Data show a decreasing trend with increasing temperature. The dashed line is the D_{In} required for core-mantle equilibrium in the Earth.

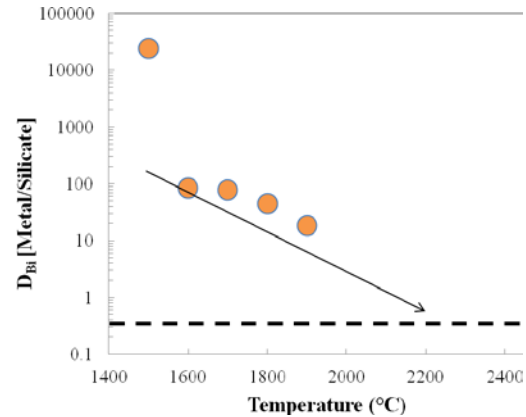


Fig.4. Partition coefficients with respect to temperature for Bi. Data show a decreasing trend with increasing temperature. The dashed line is the D_{Bi} required for core-mantle equilibrium in the Earth.

References: [1] Righter, K. et al. (2011) *Earth Planet Sci. Lett.*, 304, 158-167. [2] Albarede, F. (2009) *Nature*, 461, 1227-1233. [3] Lewis, R.D. et al. (1993) *Meteorites*, 28, 622-628. [4] Li and Agee CB. (1996) *Geochemistry of mantle-core formation at high pressure. Nature*, 381:686-689. [5] Righter K, Drake MJ. (1997) Metal-silicate equilibrium in a homogeneously accreting Earth: new results for Re. *Earth Planet Sci. Lett.*, 146:541-53

Table 1. Summary of all the MgO capsule experiments. N.D. stands for “not detected”

Sample	MgO1500	MgO1600	MgO1700	MgO1800	MgO1900
T (°C)	1500	1600	1700	1800	1900
Duration (min)	180	90	45	15	10
ΔIW	-1.77	-1.93	-2.03	-2.12	-2.33
<i>Silicate</i>					
Na ₂ O	3.98	3.59	2.62	1.99	2.92
MgO	16.5	21.1	27.6	32.1	29.2
Al ₂ O ₃	9.57	11.49	9.62	7.84	9.22
SiO ₂	29.8	28.8	30.2	30.9	32.6
P ₂ O ₅	1.06	0.83	0.77	0.49	0.36
SO ₂	0.03	0.01	0.03	0.02	0.02
K ₂ O	2.45	2.10	1.67	1.28	1.67
CaO	15.0	13.7	10.5	9.00	11.3
TiO ₂	4.29	3.92	2.96	2.55	3.08
Cr ₂ O ₃	0.01	0.02	0.02	0.01	0.01
MnO	0.16	0.16	0.14	0.13	0.11
FeO	14.7	13.0	11.7	11.1	8.70
Total	97.53	98.77	97.77	97.39	99.20
Bi ppm	1.95	5.71	10.2	16.4	63.5
In ppm	2071	1962	2222	2680	4191
Cd ppm	849	1099	1550	1577	2514
<i>Metal</i>					
Si	0.0	0.04	0.51	0.02	0.02
P	0.10	0.19	0.50	0.30	0.57
S	0.01	0.02	0.07	0.04	0.03
Fe	87.7	96.3	86.8	96.7	95.2
Cd	0.70	0.01	N.D.	N.D.	N.D.
In	2.92	0.49	0.74	0.48	0.52
Sn	0.07	0.00	N.D.	N.D.	N.D.
Bi	4.73	0.05	0.08	0.07	0.12
Total	96.25	97.06	88.72	97.64	96.48
D _{Bi}	24253.83	85.42	78.81	44.97	18.15
D _{in}	22.83	2.52	3.32	1.79	1.25
D _{Cd}	8.22	0.06	<0.06	<0.06	<0.04

THE EFFECT OF METALLICITY ON THE ATMOSPHERIC COMPOSITION OF GJ 436b. M. R. Richardson¹ and J. I. Moses², ¹Rice University, Houston, TX (mrr4@rice.edu). ²Space Science Institute, Seabrook, TX.

Introduction. The discovery of GJ 436b in 2004 by the radial velocity method [1], and the 2007 discovery of its transit [2], made this planet the first of its kind: previously, scientists had known of no transiting planets with GJ 436b’s size and mass. It was deemed a “Hot Neptune” due to its perceived similarity to our Solar System’s eighth planet. However, the GJ 436b system has little in common with ours. GJ 436b moves in an elliptical orbit only about 0.03 AU away from its host star. Since GJ 436b’s host star is an M dwarf, its luminosity is some 2% of our Sun’s [2]. Therefore, despite GJ 436b’s “Hot” title, its effective temperature is only around 700K [3].

In rare cases, the orbital plane of an exoplanet will be edge-on as seen from the Earth, and the planet can be observed to transit its host star. We can obtain information about the planet by observing the changes in flux when the planet passes in front of and behind the star [4]. In the first case, a primary transit, we can determine the size of the planet by measuring the drop in observed light from the star, which is proportional to the planet-to-star radius ratio [5][6]. In the second case, the secondary eclipse, we can detect the planet’s emission spectrum by subtracting the flux observed when the planet is behind its star from the observed flux just before and after the eclipse. The wavelength dependence of the planet’s emission tells us something about molecular absorption features, and therefore the composition, of its atmosphere.

A planet with the density and effective temperature of GJ 436b can be modeled, assuming equilibrium chemistry, in order to get a first-order determination of the makeup of its atmosphere. Knowing that the planet has to be hydrogen-rich due to its large size for its mass [5][6], equilibrium models assuming a solar-like composition reveal that methane (CH₄) should be the dominant carbon-carrier and water should be the dominant oxygen-carrier. For a normal, solar-composition atmosphere (blue line in Fig. 1), the temperature-pressure profile of GJ 436b stays strictly within the CH₄ regime at observable pressures. Methane is expected to be very abundant, as is water; however, carbon dioxide and carbon monoxide would be much less abundant. This composition is similar to the giant planets in our Solar System.

However, secondary-eclipse data reveal a composition much different than expected for GJ 436b. Spitzer Space Telescope data analyzed by Madhusudhan and Seager [7] and Stevenson et al. [8] show high flux in the 3.6-micron channel and very low flux in the 4.5-micron channel, as well as higher than expected flux in both the 5.8- and 8- μ m channels. Methane absorbs strongly in the 3.6- and the 8- μ m regions, CO in the 4.5- μ m region, CO₂ at 4.5 and 16 μ m, and water has features across all six of

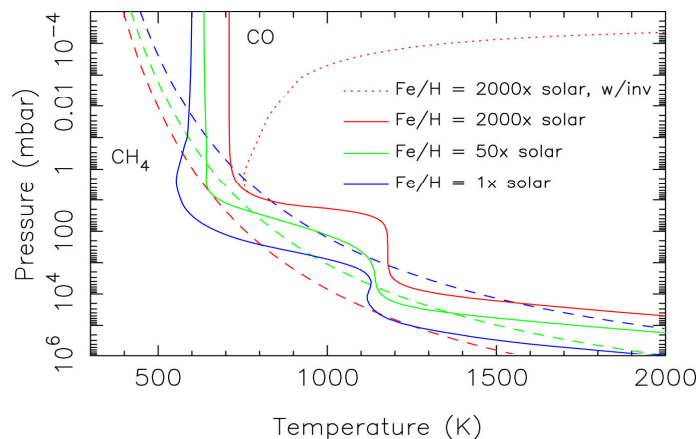


Figure 1. Temperature-pressure profiles at varying metallicities. The dashed lines represent the boundary between CO- and CH₄-dominated regimes for each metallicity. 1x and 50x solar metallicity thermal profiles are from the 3D circulation models of Lewis et al. [19]. Profiles for 500x and 2000x solar metallicity were originally estimated by shifting the Lewis et al. 50x solar profile up in altitude to account for the increased optical thickness at high altitudes, but we also manually adjusted the 2000x solar profile (red curve) to better reproduce the Spitzer spectra. We consider one 2000x solar profile with an arbitrary thermal inversion (dotted).

Spitzer’s channels. Madhusudhan and Seager [7] have derived constraints on the abundances of these four molecules from the Spitzer data. Particularly notable is their conclusion that the very high flux in the 3.6-micron channel requires an unexpectedly low methane mixing ratio of less than 10⁻⁶, to prevent too much 3.6-micron absorption. Also relevant is the high required abundance for CO, derived from the very low flux in the 4.5-micron channel, and the relatively low inferred abundance for water. These results are in stark contrast to the theoretical models that predict a methane-rich and CO-poor atmosphere of GJ 436b.

Our project focuses on rectifying the problem with the theoretically predicted composition of GJ 436b’s atmosphere. Madhusudhan and Seager [7] have suggested that disequilibrium processes, like eddy mixing and photochemistry, can account for the differences between the model and the data. However, Line et al. [9] disagree, using disequilibrium models to show that for a GJ 436b with a ratio of heavier elements to hydrogen (a measure called metallicity) similar to our Sun, or even for a metallicity 50 times solar, CH₄ will always dominate over CO.

We suggest that a very high metallicity for GJ 436b could resolve the apparent discrepancy between the observed and predicted composition. For sufficiently high metallicities with respect to solar, the temperature-pressure profile of the atmosphere tends to stay in the CO-dominated regime, instead of the CH₄ regime, as is shown in Fig. 1. In a high metallicity setting, hydrogen is less prevalent, so oxygen and

carbon will prefer to be in CO and CO₂ instead of H₂O and CH₄. Very high metallicities for gas or ice giants are not too outlandish to be considered: Neptune is observed to have a carbon-to-hydrogen ratio of 40-70x solar [10] and estimated to have an oxygen-to-hydrogen ratio of up to 440x solar [11]. We use thermochemical and photochemical kinetics models to examine the effects of varying metallicity for GJ 436b, in order to try to obtain abundances of methane and other molecules that will lead to a predicted spectrum that fits the observational data.

Procedure. Our equilibrium models are obtained by using the CEA code developed by Gordon and McBride [12] with thermodynamic parameters from Moses et al. [13]. The elements included in the model are H, He, O, C, and N.

The disequilibrium models are generated using the 1D KINETICS code of Allen et al. [14] modified as described in Moses et al. [13]. The code solves the continuity equations in the vertical direction for ~90 species and ~1800 reactions. A unique feature of this thermochemical and photochemical kinetics and diffusion model is that the reactions are fully reversed, such that, if given enough time and with no transport or dissociating ultraviolet radiation, the code would reproduce abundance profiles in thermochemical equilibrium. However, the UV photons from the planet's star can cause molecules in the atmosphere to break up, or photodissociate, and subsequent reactions drive the chemistry away from equilibrium. To simulate the UV flux incident on the planet's atmosphere, we used a composite spectrum from stars of a similar spectral type as GJ 436, like GL 15B, as well as X-ray and EUV estimates and measurements for GJ 436 (e.g. [15], [16], [17], and the STSci MAST archive at <http://archive.stsci.edu>).

In addition to photodissociation, a process called transport-induced quenching can affect an atmosphere's composition. As the temperature of the atmosphere decreases, the molecules that are ordinarily in chemical equilibrium may not have the energy to overcome the activation barrier in both the forward and backward reactions, and the time period necessary for equilibrium to be reached becomes longer. Concurrently, due to atmospheric vertical mixing, parcels of gas are carried to different altitudes, sometimes faster than they can reach equilibrium. The altitude at which the timescale for chemical reactions becomes greater than the timescale for vertical mixing is called the quench point. Above this point, abundances of the quenched species remain constant throughout large portions of the atmosphere.

We find that molecules like O₂ that are unimportant in low-metallicity models become more significant as the metallicity is increased. Because ozone could be a factor in the planet's chemistry when O₂ is abundant, we have added ozone to the model and up-

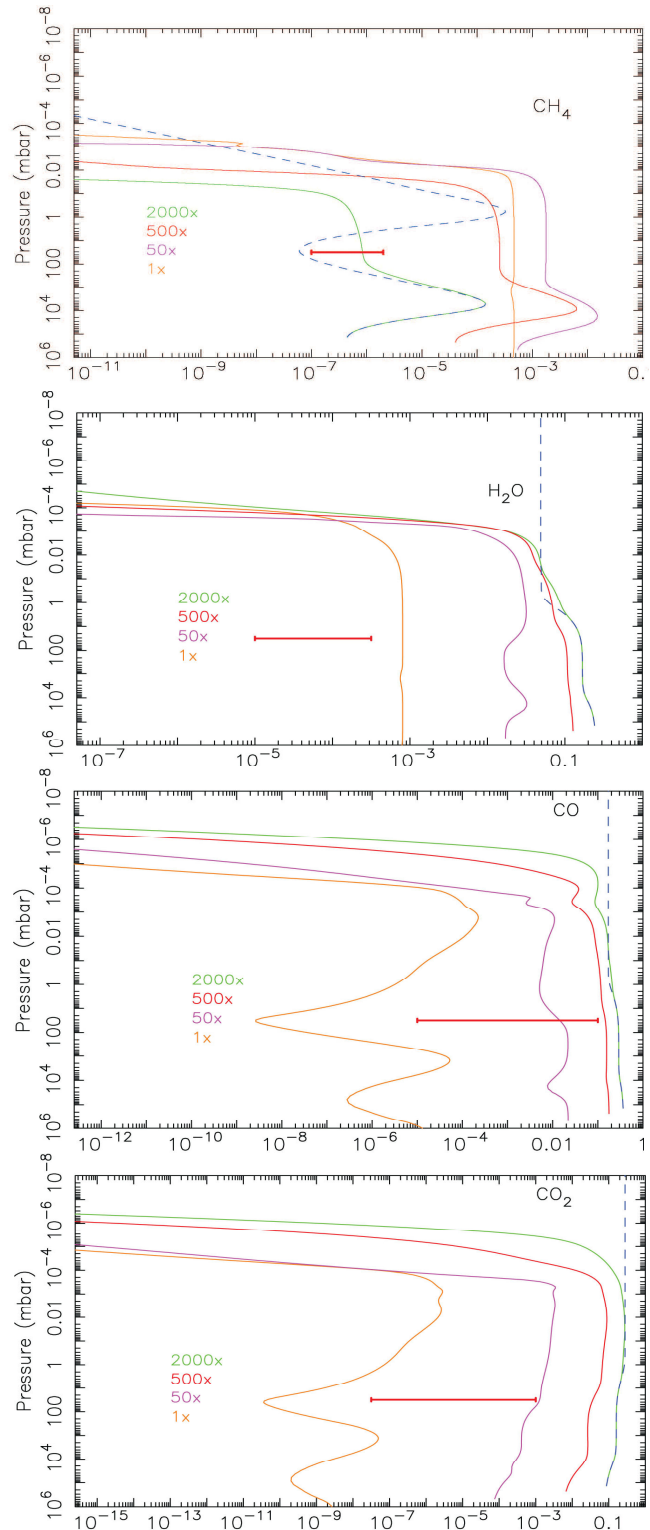


Figure 2. Modeled mixing ratios of four molecules at different metallicities as a function of pressure. The blue dashed line is a 2000x model at equilibrium. The red bar represents the constraints derived by Madhusudhan and Seager [7].

dated our photodissociation cross-sections and quantum yields for a large number of species based on ultraviolet cross-sections from the Mainz database (<http://www.atmosphere.mpg.de/enid/2295>) and compilations such as Atkinson et al. [18].

Results. Our results from the KINETICS code are shown in Fig. 2, which compares the 1x, 50x, 500x, and 2000x solar metallicity atmosphere results from our disequilibrium chemistry model and constraints obtained by Madhusudhan and Seager [7]. In order for our calculations to align with the data, the relative abundance of each molecule must compare well with these constraints.

Note that the methane compares better with the observational constraints as the metallicity increases. Its abundance at 2000x solar metallicity falls exactly within the constraints for the portion of the atmosphere at which emissions are observed. However, the CH₄ abundance in the other three models never falls within the constraints, except at much higher altitudes, where it falls off rapidly as a result of photodissociation and molecular diffusion.

Water, however, strays farther from the constraints as the metallicity is increased. At 1x solar metallicity, the H₂O abundance is one order of magnitude greater than the observational derivations, and it continues to increase as metallicity goes up. By 2000x solar, H₂O is many orders of magnitude too great.

For both CO and CO₂, the 1x model has abundances that are too low, the 50x model is nearly within the constraints, and the 500x and 2000x models are too CO- and CO₂- rich.

However, the real test of the model is the spectral comparison. Fig. 3 illustrates the predicted spectrum of our 2000x solar composition model, in comparison with the Spitzer data. Compared to a 1x solar model, the 2000x metallicity model is improved in the relative fluxes in the 3.6- and 4.5-micron channels: the

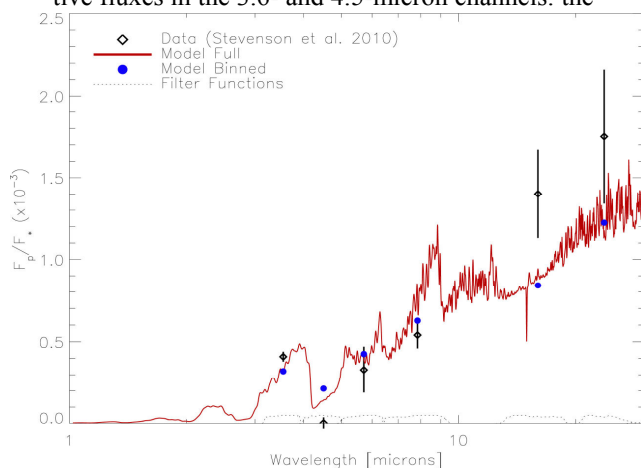


Figure 3. Model synthetic spectrum for a 2000x solar atmosphere, calculated by Michael Line (personal communication, 2012) based on the radiative transfer code described in Line et al. [9]. The blue points represent the binned averages in each channel, and the black bars are the Spitzer observations and associated error.

3.6-micron flux is higher than the 4.5-micron flux in this model, as the Spitzer observations show. However, the fluxes still lie more than 1 sigma outside the constraints for most channels, showing that this model is not perfect. Adding a thermal inversion helps the fit at long wavelengths but significantly degrades the fit at 4.5 microns and the 3.6-to-4.5-micron flux ratio.

Discussion and Conclusion. Despite our best efforts, we have not reached a point at which we are satisfied that our models can account for the observed Spitzer data. Increasing the metallicity dramatically does shift the model fluxes in the right direction, but it may be true that no matter the metallicity, some aspects of the Spitzer data will not be able to be accounted for theoretically. The extremely low methane abundance suggested by the 3.6-micron flux, for example, does not seem possible to obtain without pushing another molecule's abundance far outside of its area of constraint and moving the synthetic spectrum even further from what has been observed.

However, even if these models cannot adequately explain GJ 436b's atmosphere, they do indicate that a class of very high-metallicity hot planets may exist that exhibit compositions unlike the traditional "hot Jupiters," "hot Neptunes," or "super Earths." Hot Jupiters and Neptunes are thought to be hydrogen-rich and super Earths hydrogen-poor. Our high-metallicity models show that there may be a type of planet in between the two extremes. New possibilities for exoplanet compositions may be needed to analyze the large number of potential planets recently discovered by the Kepler mission [20]. By exploring the characteristics of a very high-metallicity atmosphere, we may contribute to the understanding of the myriad planets in our galaxy.

References. [1] Butler, R.P. et al (2004) *Astrophys. J.* 617, 580-588. [2] Gillon, M., et al (2007) *A&A* 472, L13-L16. [3] Deming, D. et al (2007) *Astrophys. J.*, 667, L199-L202. [4] Seager, S. and Deming, D. (2010) *Annu. Rev. Astron. and Astrophys.* 48, 631-672. [5] Rogers, L.A. and Seager, S. (2010) *Astrophys. J.* 712, 974-991. [6] Nettelmann, N. et al (2010) *A&A*, submitted (arXiv:1002.4447v2). [7] Madhusudhan, N. and Seager, S. (2011) *Astrophys. J.* 729, 41. [8] Stevenson, K.B. et al (2010) *Nature* 464, 1161-1164. [9] Line, M.R. et al (2011) *Astrophys. J.* 738, 32. [10] Karkoschka, E. and Tomasko, M.G. (2010) *Icarus* 205, 674-694. [11] Lodders, K. and Fegley, B. Jr. (1994) *Icarus* 112, 368-375. [12] Gordon, S. and McBride, B. J. (1994) NASA Reference Publication 1311. [13] Moses, J. I. et al (2011) *Astrophys. J.* 737, 15. [14] Allen et al. (1981) *JGR* 86, 3617-3627. [15] Sanz-Forcada, J. et al. (2011) *A&A* 532, A6. [16] Ehrenreich, D. et al. (2011) *A&A* 529, A80 [17] Heap, S.R. and Lindler, D. (2010) *Bull. Am. Astron. Soc.* 42, 494. [18] Atkinson, R. et al. (2004) *Atmos. Chem. Phys.* 4, 1461-1738. [19] Lewis, N. K. et al. (2010) *Astrophys. J.* 720, 344-356. [20] Borucki, W.J. et al. (2011) *Astrophys. J.* 736, 19.

GEOLOGICAL MAP OF THE NECTARIS BASIN AND ITS DEPOSITS. M. C. Smith¹ and P. D. Spudis², ¹East Tennessee State University, 807 University Pkwy., Johnson City, TN 37604 (smithmc2@gmail.com), ²Lunar and Planetary Institute, 3600 Bay Area Blvd., Houston, TX 77058.

Introduction: Geological maps are an efficient way to visually convey geological data in a concise manner. These maps are made in order to better understand the three-dimensional make up, geological processes, and crustal structure on any given terrestrial body. Geological maps generally provide several key pieces of information within one image: stratigraphic relationship, areal extent, and relative ages of rock units. The purpose of this project is to update the geological map of the Nectaris basin in light of new data and to unravel its stratigraphy and relation to the overlying Imbrium basin [1].

The Nectarian System, which begins with the impact that created the Nectaris basin (860 km diameter), was only proposed as a new lunar time-stratigraphic unit in 1975 [2]. Although absolute ages for this basin impact have been proposed [e.g., 3-5], no direct evidence for a specific age of Nectaris has been recovered. An objective of the Apollo 16 mission was to sample lunar material older than the Imbrium impact [6]. The subsequent mission to the Descartes highlands region, just west of Mare Nectaris, looked to be a promising location. Yet this mission returned rock samples that, arguably, could have been derived mostly from the Imbrium basin impact [1]. If we could identify Nectaris ejecta at the Apollo 16 landing site on the basis of geological or compositional affinity to such deposits elsewhere on the Moon, we would derive a better understanding of early lunar geologic history as well as address the existence or absence of a “cataclysm” in early lunar history.

A new geologic map of the Nectaris basin based upon images from the Lunar Reconnaissance Orbiter Camera (LROC) would provide better insight into the geologic units present and possibly aid in selecting a location(s) for future sample retrieval. Current lunar geologic maps were created over 30 years ago and are somewhat inconsistent in their labeling and designation of units [7-12]. The geologic map that encompasses the majority of the Nectaris basin deposits [7] was created prior

to the definition of the Nectarian System as a lunar time-stratigraphic unit [2], and therefore does not delineate Nectarian units. This new map seeks to identify and map all Nectaris basin units, including their stratigraphic relationship, areal extent, and relative age. Additionally, we hope to use this map as a template in which to determine the compositional properties of Nectaris basin ejecta as well as to interpret the samples from the Apollo 16 landing site.

Methods: A special orthographic Nectaris-centered (16°S, 34°E) basemap was made from the LROC Wide Angle Camera (WAC). Geological units were defined and mapped by surface morphology, albedo, and relative preservation. Units were distinguished and mapped using the standard methods of planetary geological mapping, including truncation of older units by younger ones, superposition and overall crater density [13]. Descriptions and labels of units were adopted and modified from previous maps where applicable [7-12]. In many cases, the Lunar Orbiter and Apollo photographs were analyzed in order to gain more insight into the reasoning behind the original geologic interpretations. Comparison of the images from Lunar Orbiter and LROC allowed for more accurate interpretations of the terrain and the geologic contacts. All craters larger than 10 km in diameter and their associated continuous ejecta blankets were mapped.

The map has been rendered in ArcMap (ArcGIS 10.0) using an “Equirectangular Moon” projection and draped over a Nectaris-centered shaded-relief image with the same projection. A color-scheme for geological units was chosen to parallel the traditional photogeologic convention for lunar units [7-12]. The map layout, including the correlation and description of units section was modeled after the most recent lunar geologic maps [1, 7-12].

Results: Units were identified and labeled ranging in age from the pre-Nectarian to the Copernican. The labeling of uncertain or unclassifiable materials as “undifferentiated”

was minimal and avoided if possible. Many geologic units originally considered Imbrian in age seem to be Nectarian, as evidenced by the superposition of Imbrian ejecta on Nectarian materials. Material previously identified as “Imbrian hilly” (Ih) and “Imbrian hilly and furrowed” (Ihf), appears to be Nectarian in age as evidenced by the superposition of smaller Imbrian chains and ejecta not visible with the resolution of the LO4 photographs.

Several locations of potential Nectaris basin impact melt-sheet remnants were identified; relatively smooth plains units lying between Nectaris basin massifs and other terra are prime candidates. Typical structures of melt-sheet remnants, such as the folding, flow features, and cooling fractures seen in the Orientale basin impact melt sheet [7] are not readily apparent at Nectaris.

Discussion: The Nectaris basin ejecta blanket (units Ntp and Nj) is manifested primarily through exposures to the south and southeast. Additional remnants of a Nectaris basin ejecta blanket (unit Nh) may be found to the west, encompassing the Apollo 16 landing site. Although this unit differs texturally from the south and southeast locations, it may be indicative of structural variations in the target rock or the superposition of Imbrium basin structure. Unit Ihp, a hilly and pitted material, spans across the Nectaris basin, but does not appear beyond the eastern rim. This unit, which may be part of the Imbrium ejecta blanket, loosely forms a fan shape, radial to Imbrium basin. It can be observed blanketing the rims of Nectarian and older craters, but not Imbrian age craters. Similarly, the Nectarian equivalent, unit Ntp, is found to blanket only the rims of pre-Nectarian craters.

Lineated material (unit NpNI) to the northwest of Nectaris basin is likely the result of the Imbrium impact. Nectarian, or even pre-Nectarian, crater remnants are scoured by troughs that are radial to Imbrium. These troughs may be caused by low-altitude, high velocity Imbrium basin ejecta ripping through older terrain.

Much of the north, northeast, east, and to some extent, far western regions surrounding the Nectaris basin display minimal evidence of its

creation. Nectarian plains material (Np), a unit consisting of hillier and more heavily cratered material than its Imbrian equivalent, can still be found on the crater floors of many Nectarian and pre-Nectarian age craters and in a larger area southwest of the crater Theophilus.

Nectarian age crater chains and clusters occur in many locations, although a large concentration of chains radial to Nectaris is evident to the southeast within the Nectaris basin Janssen Formation (Nj) (Fig. 1). These chains (Nbc) are radial to the Nectarian-age basin from which they originated and were probably caused by low angle secondary ejecta from the basin-forming impact. In most cases, the chains are partly buried by superposed Imbrian or younger material.

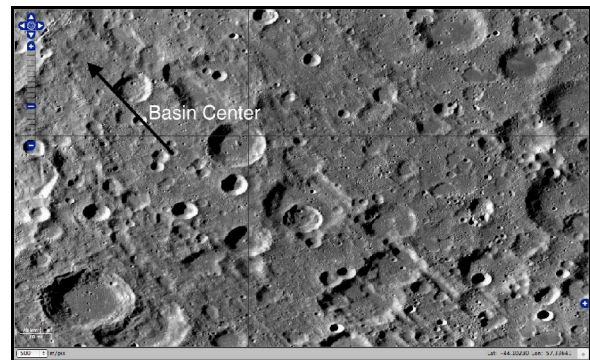


Figure 1: Nectaris basin crater chains within Janssen Formation; Basin center in direction of arrow. Image taken from ACT-REACT QuickMap.

Several sites containing possible Nectaris basin impact melt have been identified. Impact melt samples will provide the most valuable samples from which the actual age of the Nectaris impact event could be determined. Establishing this date is critical to our understanding of lunar history [1] and would solidify the time of the beginning of the Nectarian period. The ideal candidate sites generally consist of moderate to heavily cratered, higher albedo plains material situated among rugged Nectaris basin material. In some cases, the potential melt sites are perched on uplifted basin rock and occupy local topographic lows (Fig. 2). Although in some cases these areas are located adjacent to maria, they are brighter and more heavily cratered and thus they are readily differentiated from maria.

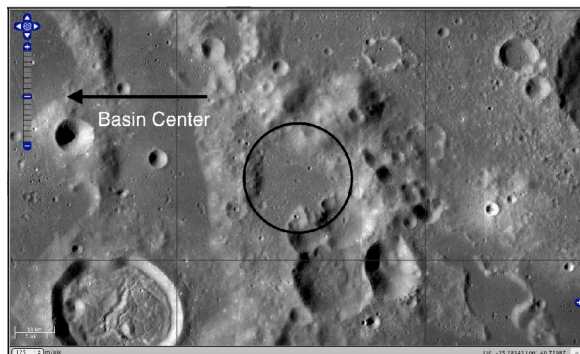


Figure 2: Probably Nectaris basin impact melt deposits near the crater Bohnenberger. Image taken from ACT-REACT QuickMap.

Summary: We have produced an updated, finely detailed geologic map of the Nectaris basin and its surrounding terrain (Fig.3) by studying and mapping from the high-resolution images of the LROC WAC global basemap and Lunar Orbiter photographs. Several units previously considered “undifferentiated” were classified and assigned stratigraphic positions. Sites that may contain Nectaris basin impact

melt were identified and recorded. These sites could prove to be desirable targets for future lunar missions, since melt samples could directly determine the absolute age of the Nectaris basin-forming impact.

References: [1] Wilhelms D.E. (1987) USGS Prof. Paper 1347. [2] Stuart-Alexander D. and Wilhelms D.E. (1975) JRUSGS 3, 53. [3] James O.B. (1981) PLPSC 12B, 209. [4] Spudis P.D. (1984) PLPSC 15, JGR 89, C95. [5] Stoffler D. et al (1985) PLPSC 15, JGR 89, C449. [6] Wilhelms D.E. (1993) To A Rocky Moon. Univ. Arizona Press [7] Wilhelms D.E. and McCauley J.F. (1971) USGS Map I-703 [8] Scott D.H. et al. (1977) USGS Map I-1034 [9] Wilhelms D.E. and El-Baz F. (1977) USGS Map I-948 [10] Stuart-Alexander D.E. (1978) USGS Map I-1047. [11] Lucchitta B.K. (1978) USGS Map I-1062. [12] Wilhelms D.E. et al. (1979) USGS Map I-1162. [13] Wilhelms D.E. (1972) USGS Astrogeol. 55

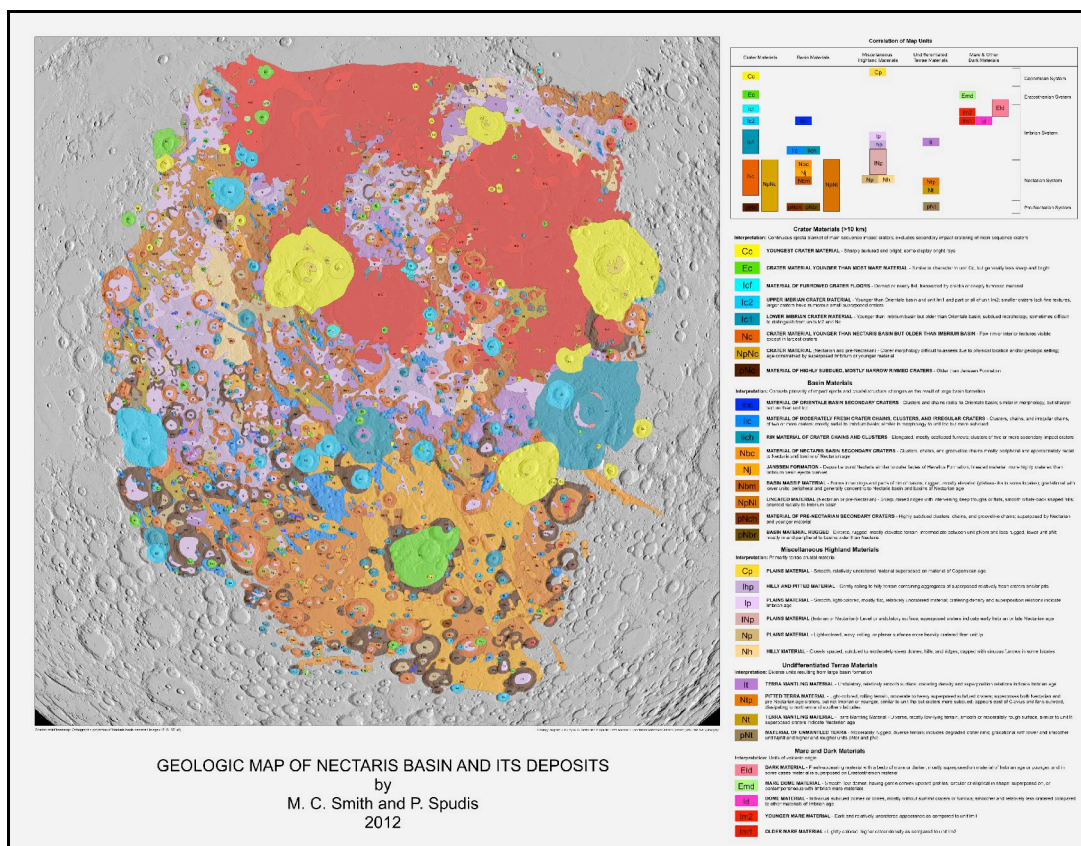


Figure 3: Geologic map of Nectaris basin and its deposits

EXTRACTION OF METEORITIC METALS FROM LUNAR REGOLITH

Jayashree Sridhar^{1,2} and B. L. Cooper², ¹Department of Aeronautics and Astronautics, HIT, (sridhar@lpi.usra.edu),
²NASA Johnson Space Center 2101, NASA Parkway Houston, Texas 77058

Introduction: The aim of this research is to develop and test ways to magnetically separate meteoritic metals from the lunar soil. To our knowledge, no other attempts have been made to accomplish this. The task would seem daunting because meteoritic metals are not the only magnetically-susceptible materials in lunar soil. It is known {Lindsay} that pure metallic iron exists in the soil in the form of nanophase iron globules (npFe⁰) in the rims of soil grains, and that lunar soil as a whole seems to be magnetically susceptible { Taylor et al,2005}. Moreover, while the amount of pure meteoritic metal increases with decreasing grain size { Basu et al; 2002; Taylor et al; 2001, 2003}, the amount of npFe⁰ also increases with decreasing grain size [1], making separation difficult.

Experimental Set-up: Our experiments involved placing magnets of various strengths at varying distances from a lunar soil sample which was immersed in isopropanol (IPA). In most tests, magnets were arranged in a horizontal plane with the side arm of a modified Dean-Stark apparatus (Figure 1), which was filled to a level slightly above the side-arm with IPA. The stopper of the side-arm held a piece of carbon tape.

The arrangements were held 30 minutes to one hour, after which the carbon tape was removed and prepared for SEM examination. Scanning Electron Microscope (SEM) studies were performed and the amounts of meteoritic metal and npFe⁰-rich grains were determined by grain counting.

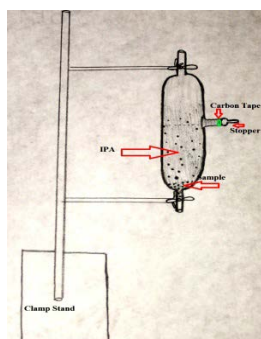


Figure 1. Experimental Set-up

Magnet Configurations:

1) Use of 2 Magnets Immersed in IPA with Sample

- Select a strong and weak magnet.
- Place them in a glass container after covering the magnets with plastic paraffin film.
- Add 2 mg of lunar dust.
- Remove the magnet after approximately two days and allow it to dry.
- Take the carbon tape and place it over the magnet recovered from the glass container.
- SEM study.
- This configuration was used only once.
- Two samples were collected; one from the strong magnet and one from the weak magnet.

2) Use of a Single Magnet outside the Glassware

- A modified Dean-Stark apparatus is used in this set-up (hereafter referred to as “glassware”—see Figure 1).
- Glassware is filled with IPA.
- Sample is pipetted into the glassware.
- Carbon-tape is mounted on to the stopper inside the glassware.
- Magnet is attached to the stopper externally.
- After two hours, the carbon tape was placed in the vessel, held for 15 minutes, then removed for study.
- This configuration was used twice and collected two samples.
- SEM study.

3) Use of a Single Magnet at a distance of 3.5 centimeters

- The glassware procedure remains the same.
- In this arrangement the magnet is placed 3.5 centimeters away from the carbon tape.
- After two hours, the carbon tape was placed in the vessel, held for 15 minutes, then removed for study.
- SEM study.
- This configuration was used only once, and one sample was collected.

4) Use of 4 magnets (2 stronger magnets and 2 weaker magnets)

The procedure remains the same except for the arrangement of the magnets (Figure 2). This

configuration was used with four starting materials to collect a total of 12 samples:

1. Size-fractionated dust (median diameter 3.0 micrometers) from lunar soil 14003,96.
2. Material ground to a median size of 2.2 micrometers from lunar soil 14003,96
3. Size-fractionated dust (median diameter 1.47 micrometers) from lunar soil 14003,96.
4. Bulk sample 12003,182 (median diameter 16.5 micrometers).

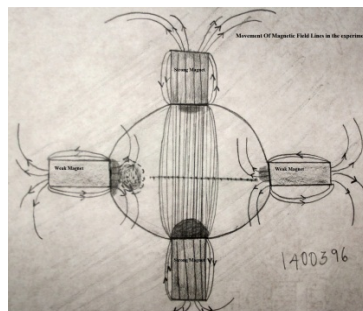


Figure 2. Magnetic field lines in final experimental set-up.

The configurations, samples used, run numbers, and data obtained are given in Table 1.

RESULTS

Magnet Configurations:		Samples	Run #	MM Grains	# of Grains with npFe ⁰
Test 1:- Use of 2 Magnets Immersed in IPA with Sample	Size-fractionated dust (median diameter 3.0 micrometers) from lunar soil 14003,96.	Strong magnet		50	251
		Weak magnet		16	88
Test 2:- Use of a single magnet outside the glassware	Size-fractionated dust (median diameter 3.0 micrometers) from lunar soil 14003,96.	1		4	14
		2		7	6
Test 3:- Use of a magnet at 3.5 cm	Size-fractionated dust (median diameter 3.0 micrometers) from lunar soil 14003,96.	1		7	6
4: Use of 4 magnets (2 stronger magnets and 2 weaker magnets)	Size-fractionated dust (median diameter 3.0 micrometers) from lunar soil 14003,96.	1		0	0
		2		0	0
	Material ground to a median size of 2.2 micrometers from lunar soil 14003,96	1		155	22
		2		0	0
		3		11	14
		4		0	0
	Size-fractionated dust (median diameter 1.5 micrometers) from lunar soil 14003,96.	1		61	9
		2		2	2
		3		4	2
		4		5	4
	Bulk sample 12003,182 (median diameter 16.5 micrometers).	1		9	2
		2		n.d.	n.d.
		3		11	8

Discussion: Nano-phase iron particles in the samples were distinguished by the spherical globules with a strong iron signature in the sample. If we were uncertain as to whether a particle contained npFe⁰ grains, we looked at the size (they should be less than 30 nanometers diameter) and their shape. Figure 5 shows an example of some of the grains with npFe⁰ that we found.

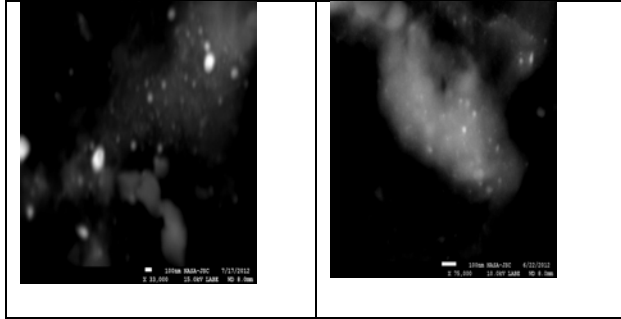


Figure 3:- SEM-images of Nano-phased iron -particles. The bright-tiny white Spots represent the nano-phased iron-particles.

Test 1:- Use of 2 Magnets Immersed in IPA with Sample

During the first test, both the strong and weak magnets collected more grains with npFe^0 than grains of meteoritic metal. Moreover, the second run collected fewer total particles than the first; however, the relative amounts collected were similar (17 to 15% meteoritic metal as a percentage of total grains counted).

Test 2:- Use of a single magnet outside the glassware

In the second test, we saw slightly more meteoritic metal (22% of the total)

Test 3:- Use of a magnet at 3.5 cm

In the third test, much more meteoritic material was collected compared to npFe^0 -enriched grains—54% of the total.

Test 4: Use of 4 magnets (2 stronger magnets and 2 weaker magnets)

The first attempt with this configuration was unsuccessful because the meteoritic material and npFe^0 -enriched grains had been removed from the sample to a significant degree. It was visually apparent that the sample was lighter in color than the starting material, thus it was decided to try other materials with this configuration. Material ground to a median size of 2.2 micrometers from lunar soil 14003,96 was used (Cooper et al., 2009).

For the first run with this new material, the particles collected consisted of 88% meteoritic metal. In the second run, few grains were found, possibly because the carbon tape was in contact with the sample for an insufficient amount of time. There were also particles in this sample that were not lunar-like. We determined that some contamination had occurred. In the third run, the percentage of meteoritic metal was 44%; however, the overall particle count was also much reduced in this case (25 grains instead of 177 seen in the first run). This was confirmed by the total absence of grains collected on the carbon tape in run 4.

We next used another size fraction from 14003,96; in this case with a median diameter of 1.5 micrometers. In this case, on run #1, 87% of the grains were

meteoritic metal. We observed again the reduction in the total number of grains from after the first run, and the simultaneous decrease in the percentage of meteoritic metal seen in the samples.

The final sample used with this configuration was bulk soil 12030,183, median diameter 16.5 micrometers. In the first run, fewer particles were collected than had been seen in other “first runs”. In other cases the sample had produced significantly more grains when it was first used. In this case, the first run collected only 11 particles—however the percentage of meteoritic metal was again quite high: 82%. We obtained no data from the second run because the carbon tape was torn during removal from the glassware. On the third run, again only a few grains were collected (19); and in this case, the percentage of meteoritic metal was reduced to 58%, a reduction which is consistent with the other samples. It should also be noted that this sample had the largest median diameter of any of the samples tried. This may in part explain the dearth of small particles on the carbon tape.

Conclusions: -

Experimental results indicate promise for the extraction of meteoritic metals from lunar regolith. However, these preliminary results do not address all of the obstacles that would be found in attempting this procedure on an industrial scale. More work is needed to refine the technique and understand more about the variables that affected our results.

Acknowledgements: This work evolved from my internship at NASA-Johnson Space Center in Planetary dust lab and Scanning electron Microscope facility. I have also referred several research works for doing this paper. I would like to thank my advisor Dr. Bonnie Cooper for giving me support and encouragement. I also extend my gratitude to Dr.Dave McKay and Dr.Daniel Ross.

References:

[1] Sarah K. Noble, Cake M. Pietersi, Lawrence A. Taylor, Richard V. Morris, Carlton C. Allen, David S. McKay and Lindsay P. Keller “The optical properties of the finest fraction of lunar soil: Implications for space weathering “*Meteoritics & Planetary Science* 36, 3 1-42 (2001).

[2]Lawrence.A.Taylor, Harris.H.Schmitt, W.David Carrier, Masami Nakagawa, “Lunar Dust: - Liability to Asset” AIAA 2005-2510.

PARTICLE SIZE DISTRIBUTION OF THE ALLENDE CV3 CHONDRITE: A STUDY THAT SPANS DECIMETER TO MICROMETER SCALES. P. Srinivasan¹ and J. I. Simon², ¹Rutgers University, Department of Earth and Planetary Sciences, Piscataway, NJ 08855, psriniv@pegasus.rutgers.edu, ²Center for Isotope Cosmochemistry and Geochronology, ARES, NASA JSC, Houston, TX 77058, justin.i.simon@nasa.gov.

Introduction: Aggregate textures of chondritic meteorites reflect accretion of early-formed solid particles in the solar nebula. Understanding the characteristics of the population of particles making up individual meteorites will lead to understanding the processes by which planetary materials formed in the early Solar System (ESS). The origin(s) of particles and the size and density variations of particle populations found among chondrites is still debated. Differences could have arisen out of formation in different locations in the nebula, and/or they could have been caused by a sorting process [1]. Chondrules, particles once partially molten in the nebula, have been greatly studied due to their considerable presence in most chondrites. Nebular shocks have been proposed for making chondrules [2-3]. Modal analyses have also been acquired to understand chondrule sorting in the ESS [4-5]. Many ideas on the cause of this mechanism have been proposed; some including sorting by mass [6], by X-winds [7], turbulent concentration [8], and by photophoresis [9]. However, few similar studies have been conducted for calcium-, aluminum-rich inclusions (CAIs). These particles are known to have formed early, and their distribution could reveal a great deal about the early stages of Solar System history. Unfortunately, CAIs are not as common in chondrites as chondrules are, reducing the usefulness of studies restricted to a few thin sections. Furthermore, the largest sizes of CAIs are generally much larger than chondrules, and therefore larger CAI particles are rarely present in most studied chondrite thin sections. Rims on chondrules and CAIs can also provide great insight to early accretionary events. The mineralogy, composition, and size of the rims can provide evidence of the conditions of the nebula, such as aerodynamic sorting and timing of their formations compared to that of their hosts [10][11]. This study performs a more representative sampling of the CAI population in the Allende chondrite by investigating a two decimeter-sized slab. Our results and the measurement of rims on particles will be integrated with those obtained previously on smaller slabs at the micrometer scale [12].

Allende CV3 chondrite. Allende is classified as a carbonaceous chondrite, under the Vigarano specimen type. It has a petrologic classification of 3, meaning that it is a “least altered” sample [13]. This chondrite was later reclassified as 3.6, for reasons of slight thermal metamorphism and an effect of secondary process-

es. Allende was heated to about 550 - 600°C [14], probably resulting from shock [15] or short-lived isotopes [16]. Due to its exposure to heat, some argue that this sample is not pristine enough to study primary processes in the solar nebula, as it has encountered secondary processes. Whilst that may be true in some context, understanding the initial stages of an object is unattainable without understanding its consequential stages. Furthermore, this is less of a concern for modal analysis studies that rely on the shape and size of particles rather than their pristine compositions. CV chondrites are also vastly important due to their immense volume of chondrules, which the literature states as ~45%, and refractory inclusions at ~10%. These chondrites are also known for their particles’ relatively large diameters [9].

Methodology: For our analyses, we used a large slab of the Allende CV3 chondrite (~26 cm x 20 cm) as well as two smaller thick sections, Allende-6 and Allende-7 (~1.5 cm x 1.5 cm, each).

Macro-photographs. In order to accurately constrain the distribution of the largest CAIs in Allende, measurement of a large slab is required. In practical terms, analyses of more than 10 thin sections would be required to represent the size distribution of CAIs [17]. A large Allende slab has been located in a private collection and made available for non-destructive investigation. Our analyses mainly derive from examining particles with high-resolution digital macro-photographs (5.4µm/pixel), using a camera attached to a petrologic microscope. Both the front and back of the slab have been photographed with 1.25x magnification. Due to the roughness of the cut of the slab, this was determined to be the best magnification that focused on the individual particles. Roughly 400 images for each side were produced, and stitched together using Adobe Photoshop and Illustrator (Figure 1 A). In order to include the smallest CAI particles, and for inter-comparison purposes, two smaller pieces of Allende (Allende-6 and Allende-7) were photographed under normal light with 1.25x and 2.0x resolution (Figure 1B and 1C). These two thick sections had been studied previously by SEM [12], allowing comparison of the mineralogy of select particles to their images in normal light. This aided our determinations of which particles were CAIs, and which were chondrules in the macro-photographs. All of the CAIs on both sides of the slab have been outlined.

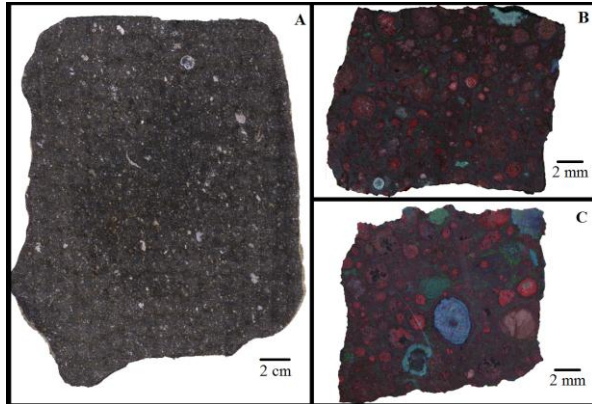


Figure 1. (A) The Allende slab under plain light. (B) and (C) Allende-6 and -7 under plain light, embedded with false-colored X-ray mineralogical data. Mg=red, Al=blue, Ca=green. Note different scales.

Figure 2 (A and B) shows two outlined CAIs, and their different textures. Since no mineralogical data has yet been taken for the slab, there will in essence be an error in the count, since some CAIs might have been spuriously excluded and some other particles might have been included. Future X-ray fluorescence (XRF) procedures, which will be later discussed, will provide invaluable information to reduce the uncertainty in these measurements.

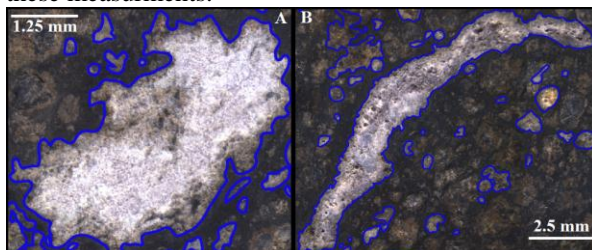


Figure 2. (A) and (B) show outlined CAIs in blue. As the images depict, CAIs come in a variety of shapes and sizes.

Rim sizes of particles. Rims post-date their hosts, by the law of superposition, and they are important in understanding the processes occurring in the solar nebula. Fine-grained rims formed from low-temperature, FeO-rich dust [16]. Coarse-grained rims are relatively FeO-rich but igneous in composition, which means that their material was at some point heated and melted [10]. These rims were clearly formed in very different conditions, and examining their sizes and textures will contribute increasing knowledge about the ESS. Analyses on rim volume provide evidence that there is a strong correlation between the host chondrule core radius [11][18-20]. Previous work has provided mineralogical data on Allende-6 and -7, as well as an outline of chondrules, CAIs, and their respective rims in both thick sections [12]. Using Illustrator, the rim sizes of the particles, keeping in mind their mineralogy and

host size, were measured. Some chondrules show multiple rims, providing evidence of the several stages that likely occurred. Some rims appear to form by accretion (e.g., accretionary rims, [10]), others by gas phase condensation [21], and some by remelting/late recrystallization [22]. The thicknesses of all rims were measured regardless of their possible origins. Figure 3 shows an example of an outlined chondrule with its surrounding rim.

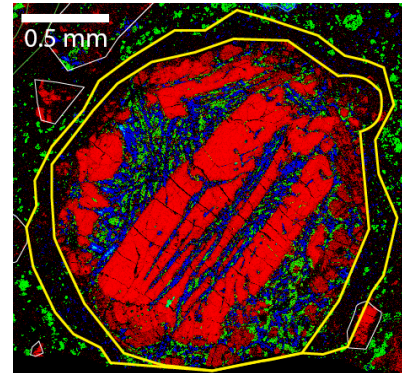


Figure 3. Barred olivine chondrule from Allende-7 with its outlined rim in yellow. Color coding of X-ray mineralogical data as in Fig. 1 B,C.

ImageJ. Outlining all of the CAIs and chondrules allows us to create a binary image of the samples (Figure 4).

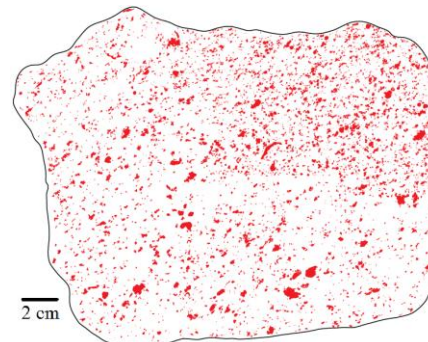


Figure 4. Binary image of CAIs in the Allende slab used to process information with ImageJ. Image shows a slight overrepresentation in the right-hand corner due to the inclusion of smaller particle sizes.

We can then use the image analysis program ImageJ to characterize the particles, in particular their size distributions. ImageJ produces data on the area of each particle, as well as its major and minor axes. For counting purposes, we excluded particles that were under $200000 \mu\text{m}^2$ in size to compensate for overrepresentation of the smaller outlined particles. This is justified because accurate identification of these smaller particles are less certain by eye. The complete size range of CAIs in Allende will be obtained by combining this

work with characterization of sub-200000 μm^2 particle size fractions obtained with SEM [17].

Results: With the help of ImageJ, we were able to produce data for the mean particle size as well as a histogram of the CAIs (Figure 5). Below lists the overall statistics:

- Mean area = 571262.96 μm^2
- Standard deviation = 708571.4 μm^2
- Min axis = 496.2 μm
- Max axis = 4119.0 μm

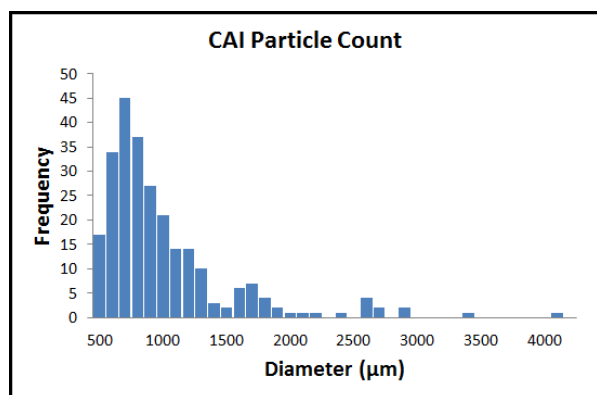


Figure 5. Particle count distribution for CAIs in the Allende slab according to diameter (in μm). Smallest particle size accounted for was $\geq 200,000 \mu\text{m}^2$.

Like chondrules in Allende [4-5], there is a much higher frequency of smaller sized CAIs than larger, which is to be expected if CAIs and chondrules were sorted by the same or similar processes. Analyses from the second side of the slab are still in progress. The particle counts for the Allende slab will soon be compared to those of the previously obtained counts on Allende-6 and Allende-7. Data obtained from chondrule rim sizes are seen below in Table 1. Additional data will also be added to the previous collection to form a greater compilation [12].

Chondrule	Rim Size (μm)	Core Radius (μm)
1	118.426	1817.670
2	49.763	751.040
3	102.721	1202.992
4	186.514	1394.477
5	140.143	771.075
6	246.715	1064.448
7	56.929	377.814

Table 1. Rim size data as compared to core radius for chondrules in Allende-6.

Discussion and Future Work: Due to the large size of the Allende slab, all data obtained from these CAIs will greatly add to the current knowledge of sorting processes in the ESS. CAIs are the oldest solids in

the solar system, and still not much is understood about how they were formed. Looking at rim sizes will also allow us to understand more about the conditions in the early solar system and possibly about incipient chondrite accretion mechanisms. If two chondrules have the same texture and same rim size, then there is a very high possibility that they were accreted in the same manner and maybe even at the same time. Having macro-photographs of the Allende slab is necessary in understanding populations of CAIs and chondrules, however, more data must be obtained as well. Using the outlined chondrules in our Allende samples, we will apply an algorithm that creates our 2-dimensional particles into 3-dimensions. This method has already been used before on chondrule particles [12] and will be helpful in determining the actual sizes of the particles. X-ray fluorescence (XRF) data will also immensely add to this project, as it will give us elemental analyses providing more robust identification of smaller particles. The XRF method has a lower spatial resolution, so already having an outline of the CAIs and chondrules is essential.

References: [1] Jones R. H. (2005) *ASP Conference Series*, 341, 251-281. [2] Rubin A. E. (2000) *Earth Sci. Rev.*, 50, 3-27. [3] Connolly H. C. Jr. & Desch S. J. (2004) *Chem. Erde*, 64, 95-125. [4] Teitler S. A. et al. (2010) *Meteoritics*, 45, 1124-1135. [5] Cuzzi J. N. et al. (2001) *APJ*, 546, 496-508. [6] Shu F. H. et al. (1996) *Science*, 271, 1545-1552. [7] Kuebler K. E. et al. (1997) *LPSC*, 28, #1366. [8] Hogen R. C. et al. (1999) *Physical Rev. E*, 60, 1674-1680. [9] Wurm G. & Krauss O. (2006), *Icarus*, 180, 487-495. [10] Krot A. N. & Wasson J. T. (1995) *Geochim. Cosmochim. Acta*, 59, 4951-4966. [11] Paque J. M. & Cuzzi J. N. (1997), *LPSC*, 28, #1189. [12] Christoffersen P. A. et al. (2011) *LPSC*, 43, #2058. [13] Van Schmus W. R. & Wood J. A. (1967) *Geochim. Cosmochim. Acta*, 31, 747-765. [14] Bonal L. et al. (2006) *Geochim. Cosmochim. Acta*, 70, 1849-1863. [15] Rubin A. E. (2005) *Sci. Am.*, 292, 80-87. [16] Scott E. R. D. (2007) *Annu. Rev. Earth Planet. Sci.*, 35, 577-620. [17] Chayes F. (1956) in *Petrologic Modal Analysis*, 1-139. [18] Metzler K. et al. (1992) *Geochim. Cosmochim. Acta*, 56, 2873-2897. [19] Sears D. W. G. et al. (1993) *Meteoritics*, 28, 669-675. [20] Metzler K. & Bischoff A. (1996) in *Chondrules and the Protoplanetary Disk* (Eds. R. H. Hewins, et al.), 153-161. [21] Petaev M. I. & Wood J. A. (2005) *Astron. Soc. Pac. Conf. Series*, 341, 373-406. [22] Clayton R. N. et al. (1983) in *Chondrules and their Origins* (Ed. E. A. King), 37.

NOTES

NOTES
